Entropy Measurements of Li-Ion Battery Cells with Li- and Mn-Rich Layered Transition Metal Oxides via Linear Temperature Variation

Journal of The Electrochemical Society, 2021 **168** 120502

Entropy Measurements of Li-Ion Battery Cells with Li- and Mn-Rich Layered Transition Metal Oxides via Linear Temperature Variation

Franziska Friedrich,[*,z] Susanne Pieper, and Hubert A. Gasteiger[**]

Chair of Technical Electrochemistry, Department of Chemistry and Catalysis Research Center, Technical University of Munich, Munich, Germany

Changes in the partial molar entropy of lithium- and manganese-rich layered transition metal oxides (LMR-NCM) are investigated using a recently established electrochemical measuring protocol, in which the open-circuit voltage (OCV) of a cell is recorded during linear variation of the cell temperature. With this method, the entropy changes of LMR-NCM in half-cells were precisely determined, revealing a path dependence of the entropy during charge and discharge as a function of state of charge, which vanished as a function of OCV. This observation is in line with other hysteresis phenomena observed for LMR-NCM, of which the OCV hysteresis is the most striking one. For a systematic investigation of the entropy changes in LMR-NCM, measurements were conducted during the first activation cycle and in a subsequent cycle. In addition, two LMR-NCM materials with different degrees of overlithiation were contrasted. Contributions from configurational and vibrational entropy are discussed. Our results suggest that the entropy profile during activation exhibits features from the configurational entropy, while during subsequent cycling the vibrational entropy dominates the entropy curve.

 [DOI: 10.1149/1945-7111/ac3938]

Manuscript submitted September 20, 2021; revised manuscript received October 26, 2021. Published December 2, 2021. *This was paper 2851 presented during PRiME 2020, October 4–9, 2020.*

Supplementary material for this article is available online

For Li-ion battery development, lithium- and manganese-rich layered transition metal oxides (LMR-NCM, $Li_{1+\delta}[TM]_{1-\delta}O_2$ with TM = Ni, Co, Mn and typically $0.1 < \delta < 0.2$), are currently under investigation as potential next generation cathode active materials (CAM). Their exceptionally high gravimetric capacity is, however, accompanied by a pronounced voltage hysteresis, of which a significant part is still present at open circuit conditions. This OCV hysteresis is a material-specific property. The hysteresis does not only affect the voltage profile, but also the cathode resistance,[1–3] the Li site occupation[4] as well as the LMR-NCM lattice parameters[5,6] and atomic distances.[7] To gain a better understanding of the thermodynamic processes upon cycling LMR-NCM cathodes, entropy measurements were conducted in this study. Hereby, the partial molar entropy, $\frac{dS}{d\xi}(\xi)$, is obtained in a sensitive, non-destructive way from the derivative of the OCV with respect to temperature. Such data complement information on free energy gained from OCV and allow for a more comprehensive characterization of thermodynamic processes in battery cells in situ.[8] In contrast to other techniques, e.g. based on diffraction, entropy is capable of monitoring even minor changes in the environment of the Li ions.

So far, the interpretation of experimental entropy data of battery active materials in the literature was mainly constricted to a quantification of the corresponding heat terms[9–11] and to a relative comparison between materials.[10–12] The shape of the entropy curve was either discussed in context of configurational entropy in studies including theoretical calculations and computational simulations[13–15] or it was ignored. Here, we present a study on entropy changes of LMR-NCM/Li half-cells and will discuss different possible contributions to the shape of the entropy curve, including configurational and vibrational entropy. To overcome systematic experimental errors, a linear temperature variation method was established based on previous literature reports.[16–18] With this method, partial molar entropy changes in LMR-NCM were measured, revealing an unusual resonance-like signature, which is typical of a second order transition. The center and width of this transition differ when measured during charge and discharge and plotted as a function of SOC, while its appearance in both directions coincides when plotted against OCV. The correlation with OCV apparently reflects a Gibbs free energy driven process, which seems to be associated with only very subtle structural changes, since it escapes observation by other techniques so far. Due to the strong dependence of the entropy on the OCV rather than on the Li content, any significant contribution of configurational entropy can be discarded in LMR-NCM. We thus consider vibrational entropy being dominant in LMR-NCM.

Theoretical Considerations

The focus of this study is on the thermodynamics of the Li (de-) intercalation processes of LMR-NCM, which for simplicity is abbreviated as NCM in the following equations. The commonly used structural formula of LMR-NCM ($Li_{1+\delta}[TM]_{1-\delta}O_2$, TM = Ni, Co, Mn) was simplified to $Li_y[TM]_zO_2$, where y describes the amount of lithium in the cathode active material (CAM) and where the maximum value of y is equal to $1+\delta$, as explained in the Experimental section. To simplify the investigated cell chemistry, Li metal is used as a counter electrode, giving the following reactions for the positive and negative electrodes during discharge:

Positive electrode:

$$Liy[TM]_zO_2 + x\,Li^+ + xe^- \xrightarrow{\text{discharge}} Li_{y+x}[TM]_zO_2 \quad [1]$$

Negative electrode:

$$x\,Li \xrightarrow{\text{discharge}} x\,Li^+ + x\,e^- \quad [2]$$

For the whole cell reaction during discharge ($\Delta G < 0$), it follows:

$$Li_y[TM]_zO_2 + x\,Li \xrightarrow{\text{discharge}} Li_{y+x}[TM]_zO_2 \quad [3]$$

Thereby, the electrons supplied on discharge at the negative electrode are transferred to the positive electrode via the external

*Electrochemical Society Student Member.
**Electrochemical Society Fellow.
[z]E-mail: franziska.friedrich@tum.de

circuit. For the charge reaction, the direction is reversed and $\Delta G > 0$.

The overall stoichiometric amount of Li can be summarized as $x_{Li} = x + y$. For the Li- and Mn-rich NCM used herein, the maximum value of x_{Li} is $1 + \delta$ as explained in the Experimental section. To describe the progress of the charging/discharging reaction, we will use the reaction turnover parameter ξ, which we define as $\xi = (1 + \delta) - x_{Li}$. It runs parallel to the SOC but is normalized in stoichiometric units. ξ is zero for a fully lithiated (pristine) CAM and 1.14 for a completely delithiated (charged) 0.33 LMR-NCM. Since it increases on charging (deintercalation of the LMR-NCM) and decreases on discharging, the sign of $d\xi$ explicitly reflects the direction of the reaction.

The partial molar entropy $\frac{dS}{d\xi}(\xi)$**.—**dS is the change in the total entropy of a cell with 1 mol of cathode material on charging with a differential amount of electrons $d\xi$ and thus releasing the same amount of Li^+. For the half-cell reaction at the cathode side, the corresponding molar entropy change can be expressed as follows:

$$dS_{cha,cathode}(\xi) = \frac{dS_{NCM}(\xi)}{d\xi}d\xi + \frac{dS_{solv}}{d\xi}d\xi \quad [4]$$

Here, $\frac{dS_{NCM}(\xi)}{d\xi}$ describes the entropy change when a differential amount of Li^+ (corresponding to $d\xi$) is extracted from 1 mol of LMR-NCM, at an SOC at which a molar fraction ξ (of Li^+) was already extracted. We may likewise call $\frac{dS_{NCM}(\xi)}{d\xi}$ the partial molar intercalation entropy. The molar entropy of Li^+ solvation, $\frac{dS_{solv}}{d\xi}$, is the second contribution to the entropy change at the cathode interface since for any amount of Li^+ ($=d\xi$) extracted from the CAM, a corresponding number of Li^+ ions will be transferred to the electrolyte.

On the Li metal anode side, the molar entropy change upon charge is the sum of the entropy change for depositing Li at the metal anode and the entropy of desolvation of the Li^+ ions:

$$dS_{charge,anode}(\xi) = \frac{dS_{Li}}{d\xi}d\xi + \frac{dS_{desolv}}{d\xi}d\xi \quad [5]$$

In this study, entropy is measured vs a Li reference electrode. Since the Li reference electrode is practically unaffected in quantity and thus not altered in quality, its entropy is independent of the SOC.[19,20] $\frac{dS_{Li}}{d\xi}$ is the change in entropy for adding 1 mol of Li to the Li metal anode.

For the whole cell reaction shown in Eq. 3, the differential change of the total entropy of the battery for the charging process, dS_{charge}, results from the combination of Eqs. 4 and 5. By assuming a negligible concentration gradient in the electrolyte, the entropy of solvation at the cathode is counterbalanced by the desolvation of Li^+ at the Li anode and the entropy of solvation/desolvation cancel.

$$dS_{charge}(\xi) = \frac{dS}{d\xi}(\xi)d\xi = \frac{dS_{NCM}(\xi)}{d\xi}d\xi - \frac{dS_{Li}}{d\xi}d\xi \quad [6]$$

Note that only the contribution from the cathode, $\frac{dS_{NCM}(\xi)}{d\xi}$, is expected to change with ξ (SOC).

In order to clarify sign conventions pertaining to our results, we will briefly sum up how $\frac{dS}{d\xi}(\xi)$ can be derived from a temperature dependent OCV (TD-OCV) measurement. First, we correlate changes of Gibbs free energy, dG, with the electrical work reversibly stored in the cell while charging:

$$dG = dw_{el,rev} = E_0(\xi)\cdot dq \quad [7]$$

If n is the net electric charge on the ion ($n = +1$ for Li^+), n mole of electrons will have to be transported from the external power source at each turnover ξ yielding: $dq = n\cdot F\cdot d\xi$. Here, F is the Faraday constant and E_0 is the OCV. Since we have chosen $d\xi$ to be positive on charging and since in that case work will be stored in the battery and should be counted positive, according to thermodynamic convention, we get:

$$dG(\xi) = n\cdot F\cdot E_0(\xi)\cdot d\xi \quad [8]$$

Note that a negative sign would appear on the right hand side if one used dx_{Li} instead of $d\xi$, as is often found in the literature.

According to the fundamental thermodynamic relation, the entropy can be derived from the temperature dependence of the Gibbs free energy:

$$\frac{dG}{dT}(T, p, \xi)|_{p,\xi} = -S(T, p, \xi)|_{p,T} \quad [9]$$

We obtain the partial molar values of G and S by combining Eqs. 8 and 9, and dividing by $d\xi$: $\frac{d}{dT}\left(\frac{dG}{d\xi}(\xi)\right) = -\frac{dS}{d\xi}(\xi)$. This finally gives:

$$\frac{dS}{d\xi}(\xi)\,|_{p,T} = -n\cdot F\cdot\frac{d}{dT}E_0(\xi)\,|_{p,\xi} \quad [10]$$

The entropy change due to a differential increase of the turnover parameter on the left side corresponds to a temperature induced change of E_0 measured at a constant ξ. Note that the differential increase of G (endergonic for charging) due to $d\xi$ is already implicitly included in E_0. In our study, an increase in temperature was found to decrease the OCV, independent of whether the OCV was measured after charging or discharging and at all values of ξ. $\frac{\partial E_0}{\partial T}$ is thus negative and accordingly the partial molar entropy is always positive. As a consequence, the entropy of the cell increases on charging $dS = \frac{dS}{d\xi}(\xi)\cdot d\xi > 0$ because $d\xi > 0$ and vice versa decreases while discharging ($d\xi < 0$).

Depending on the electrode properties, $\frac{dS}{d\xi}(\xi)$ can change with ξ since for most electrode active materials, such as LMR-NCM, the structural and energetic properties change upon lithiation. As mentioned above, for the Li anode, the partial molar entropy can be assumed to be constant. Hence, for a LMR-NCM/Li cell, any changes of the partial molar entropy of the cell are exclusively governed by the properties of the cathode, while the value (and sign) of $\frac{dS}{d\xi}(\xi)$ includes the constant contribution from the Li anode.

The total molar entropy change $\Delta\mathbf{S}(\xi)$**.—**When we start at an SOC value "a" (ξ_a) and charge or discharge to get to state "b" (ξ_b), the total entropy change referred to 1 mol of CAM is obtained by integrating the partial molar entropy of this process, as long as local reversibility is given:

$$\Delta S = S(\xi_b) - S(\xi_a) = \int_{\xi_a}^{\xi_b}\frac{dS}{d\xi}(\xi)d\xi = \Delta S_{NCM,\,a\to b} - S_{Li} \quad [11]$$

Thereby, the total molar entropy change ΔS is a measure of additional energetic disorder in the whole battery induced by (dis-) charging the cell by $\Delta\xi$. It contains the contribution from the cathode ($\Delta S_{NCM,a\to b}$) and the Li anode (S_{Li}). Basically, there are three possible contributions to ΔS and hence to its derivative $\frac{dS}{d\xi}(\xi)$: The configurational, vibrational, and electronic entropy, which will be discussed in the following.

The electronic molar entropy change $\Delta\mathbf{S_{elec}}(\xi)$**.—**$\Delta S_{elec}(\xi)$ is associated with thermal disorder in electronic states near the Fermi

level and can be sensitive to the SOC. It can be calculated from the change of electronic density of states at the Fermi level with changing degree of lithiation. For Li_xCoO_2, it was shown that $\Delta S_{elec}(\xi)$ is negligible.[20] Since for our system, electronic entropy calculations are not available, for the time being we neglect such contributions at room temperature.

The Li-configurational molar entropy change $\Delta \mathbf{S_{config}}(x)$.—The Li-configurational entropy gives information about the distributional variability of Li atoms in the host structure. In a very simplified ideal solid solution model with Li atoms moving freely between a given number of empty sites, without changing interactions (among each other and with the host lattice), the molar entropy change is given by:

$$\Delta S_{config}(x) = -R\cdot\{x\cdot\ln x + (1-x)\cdot\ln(1-x)\} \quad [12]$$

Here, R is the molar gas constant and x the relative amount of exchangeable sites being occupied. When describing a simplified CAM, we assume the maximum number of x to be equal to one (as common for typical layered oxides but not for the LMR-NCM used in our study). Resulting from Eq. 12, $\Delta S_{config}(x) = 0$ for an 'empty' electrode ($x = 1$) and a completely filled electrode ($x = 0$). With increasing delithiation $\Delta S_{config}(x)$ increases and is categorically positive yielding a maximum at $x = 0.5$ with a value of $\Delta S_{config}(x = 0.5) = R\bullet\ln 2 = 0.693R = 5.76\text{J/(mol K)}$. To both sides of the maximum, it symmetrically decreases to zero. In the ideal solid solution case, all Li sites are energetically equal and the interactions between the Li ions among each other and with the lattice do not change during the charge/discharge process (implying a constant value for ΔH). This leads to a practically horizontal voltage curve for such an electrode material with a maximum deflection of ≈ 17 mV at $x = 0.5$ (according to the definition of the Gibbs free energy, $\Delta G = \Delta H - T\Delta S$ and Eq. 8).

Of course there are more sophisticated models, including interactions between Li and the host structure and among the Li ions at varying distances in the host, leading to more complicated entropy curves, which can even have several maxima (here, ΔH also changes as a function of SOC).[13,14] However, these curve features must become increasingly smaller in amplitude, the more maxima are detected. All of these entropy curves are categorically positive and equal to zero at the endpoints.

The partial molar configurational entropy is the slope of the configurational entropy $\Delta S_{config}(x)$ obtained by differentiating Eq. 12:

$$\frac{\partial \Delta S_{config}}{\partial x} = -R\cdot\ln\left(\frac{x}{1-x}\right) \quad [13]$$

For the simplified solid solution model ($0 \leqslant x \leqslant 1$), it is a monotonically decreasing function starting at infinity, changing curvature at the maximum of $\Delta S_{config}(x = 0.5)$ and ending at -∞ at $x = 0$.[15] For the above mentioned models with several maxima in ΔS_{config}, the corresponding derivatives give inverse sigmoidal curves with pole signatures at their ends.[13,14] In the data presented below, there is no indication of such features.

The vibrational entropy $\Delta \mathbf{S_{vib}}(\xi)$.—Here we are interested in that part of vibrational entropy, also called phonon entropy, which is associated with changes of vibrational frequencies in the crystal lattice with the degree of lithiation. Any Li-induced changes of the vibrational density of states up to the Fermi level will lead to changes in the heat capacity (C_p) and to corresponding changes in the vibrational entropy (ΔS_{vib}).

$$\Delta S_{vib} = \int_0^T \frac{C_p(T)}{T} dT \quad [14]$$

As a rule of thumb, at room temperature, the main contribution will result from low-frequency phonons with rather large effective mass, hence from the transition metal oxide host lattice rather than from the intercalated Li atoms. On the other hand, the Grüneisen relation suggests that increased stiffness should reduce C_p, yielding lower lattice entropy. Such lattice strain may be accumulated while (de-) intercalating Li from/into a host structure during charge or discharge. In particular, phase transitions occurring during charge/discharge should be mirrored in the entropy profile. Accumulation of crystallographic defects leading to disruptions of long range vibrations are expected to influence vibrational entropy. Such changes can be induced by the intercalation of Li ions into the Li layer of LMR-NCM, but also by a change in the stiffness of the host lattice, e.g. by the oxidation/reduction of transition metals, by transition metal migration, and/or by oxygen redox. The formation of Li clusters can also modulate vibrational modes. With neutron-weighted phonon density of states (DOS) derived from inelastic neutron scattering data, the Li-induced vibrational entropies at different SOCs could be calculated for Li_xCoO_2.[20] It was shown that the difference in vibrational entropy between the relatively stiff Li_xCoO_2 lattice and the soft metallic Li anode results in a significant negative but constant contribution to the partial molar entropy of the cell, which however could not explain obvious changes of $\frac{dS}{d\xi}(\xi)$ with ξ.[20] For the further discussion it is noteworthy that, in contrast to the configurational entropy, which in the simplest case is a direct function of the SOC, the vibrational entropy is closely linked to the structure of the host lattice.

Contribution of lithium to the partial molar entropy of the cell.—The contribution of the Li counter electrode is often neglected in the literature or even assumed to be zero.[20–22] As explained above for Eq. 5, the entropy of Li is independent of the SOC[19,20] but is not zero.[20,23–25] In order to determine the contribution of Li to the overall cell-TD-OCV, spatially non-isothermal measurements were conducted, which are explained in the following. In the potentiometric measurement of the cell-TD-OCV, spatially isothermal conditions are implied, where the whole cell, i.e. both cathode and anode, are subjected to the same temperature variation. In contrast, one can take precautions to change the temperature of only one of the electrodes (the thermally working electrode) in a spatially non-isothermal arrangement (see Fig. S1 in the Supporing Information available online at stacks.iop.org/JES/168/120502/mmedia). Such asymmetric temperature changes can be applied to cells with electrochemically symmetric (identical) electrodes. Spatially non-isothermal measurements yield important entropy information pertaining to the thermal working electrode material, which is why resulting values will be denominated as electrode-TD-OCV in the following. The electrode-TD-OCV differs from the cell-TD-OCV in such a way that the temperature function of the electrode that is held at constant temperature does not contribute to the electrode-TD-OCV. However, even if it might seem that the electrode-TD-OCV value leads to the entropy of a single electrode, this is not true because the potential itself is still a cell property and not a single electrode quantity, as is always the case in electrochemistry.[23] As is shown in Eq. 15, the electrode-TD-OCV depends on three factors: (i) the actual entropy contribution of the electrode under investigation, $\frac{\partial E_0'}{\partial T}$, ($E_0'$ is the OCV between a working electrode subjected to variable temperature and a counter electrode held at constant temperature), (ii) a potential build-up due to thermal diffusion of ions in the electrolyte, the so-called Soret effect $\left\{\frac{\partial E}{\partial T}\right\}_{Soret}$, and (iii) the metal-metal junction thermocouple Seebeck effect, $\left\{\frac{\partial E}{\partial T}\right\}_{Seebeck}$.[25–27]

$$\left\{\frac{\partial E_0}{\partial T}\right\}_{\text{electrode}} = \left\{\frac{\partial E_0'}{\partial T}\right\}_{\text{working electrode}} + \left\{\frac{\partial E}{\partial T}\right\}_{\text{Soret}} + \left\{\frac{\partial E}{\partial T}\right\}_{\text{Seebeck}} \quad [15]$$

When using a symmetrical Li/Li cell, the pure entropy contribution $\frac{\partial E_0'}{\partial T}$ of the Li electrode can in principle be determined from Eq. 15 if the effects (ii) and (iii) can be minimized or determined as good as possible. The thermocouple effect (iii) can be estimated from the Seebeck coefficients of the materials, which are exposed to a temperature gradient. For the symmetrical Li/Li cell, this is nickel, since only at the nickel tab of the Li electrode a changing temperature gradient will build up. With $-18.0\ \mu V\ K^{-1}$,[28] the Seebeck effect of nickel is negligibly small in comparison to the measured electrode-TD-OCV of Li, $\{\frac{\partial E_0}{\partial T}\}_{Li} = 1.12\ mV\ K^{-1}$. Furthermore, the Seebeck effect can be minimized by keeping all other metal-metal junctions isothermal.[26,27] The Soret effect describes a mass separation induced by a temperature gradient.[29,30] In the context of this study, the Soret effect plays a role in the spatially non-isothermal configuration, because a temperature-induced concentration gradient will cause a potential difference between the hot and the cold side, i.e. $\left\{\frac{\partial E}{\partial T}\right\}_{Soret}$. Comprehensive data of the Soret effect are lacking in the literature because experimental measurements of the thermodiffusion coefficient prove to be difficult and there is no universal technique to measure the Soret effect of binary mixtures.[29] In the Results part, we estimate the influence of the Soret effect on the value of the electrode-TD-OCV as rather insignificant, especially in comparison to other sources of error (cell to cell variation, accuracy of the temperature measurement, etc). This is in accordance with the "negligible thermal diffusion potential assumption" made by Swiderska-Mocek et al.[25]

Experimental

Electrode preparation.—Li- and Mn-rich layered oxides (LMR-NCM) with two different degrees of overlithiation were obtained from BASF SE (Germany). According to the notation $Li_{1+\delta}[TM]_{1-\delta}O_2$ for the pristine LRM-NCM cathode active materials, the here examined LRM-NCM materials have $\delta = 0.14$ and $\delta = 0.20$; this corresponds to a composition of $0.33\ Li_2MnO_3 \cdot 0.67\ LiTMO_2$ (for $\delta = 0.14$; further on referred to as 0.33 LMR-NCM) and $0.50\ Li_2MnO_3 \cdot 0.50\ LiTMO_2$ (for $\delta = 0.20$; further on referred to as 0.50 LMR-NCM) in the two-phase notation applied by Teufl et al.[31] (with TM = Ni, Co, Mn). The 0.33 LMR-NCM is the same material as used in previous studies of our group[6,32] and has the composition $Li_{1.14}[Ni_{0.26}Co_{0.14}Mn_{0.6}]_{0.86}O_2$. The 0.50 LMR-NCM is a follow-up batch with similar composition and properties as the material used by Teufl et al.[31]

For inks of the 0.33 LMR-NCM cathode active material, 92.5 wt% LMR-NCM (BASF SE, Germany), 3.5 wt% polyvinylidene-fluoride binder (PVDF, Kynar, HSV 900, France), and 4 wt% conductive carbon (Super-C65, Timcal, Switzerland) were dispersed in N-methyl pyrrolidine (NMP, anhydrous, Sigma-Aldrich, Germany) and mixed in a planetary orbital mixer (solids content $\approx$ 54 wt%; Thinky, USA). The resulting ink was coated onto aluminum foil ($\approx$ 15 μm, MTI, USA) and the dried coatings were calandered (GK 300 L, Saueressig, Germany) to a porosity of $\approx$ 42–45%. For electrochemical testing, electrodes with a diameter of 11 mm (for Swagelok T-cells) or 14 mm (for 2032-type coin-cells) were punched out and dried at 120 °C under dynamic vacuum for at least 12 h (Büchi, Switzerland). The loading of the 0.33 LMR-NCM cathode active material (CAM) was $\approx$ 12 mg cm^{-2}, corresponding to $\approx$ 3 mAh cm^{-2} (based on a nominal reversible capacity of 250 mAh g_{CAM}^{-1}). For experiments with the 0.50 LMR-NCM material, an industrially manufactured coating was obtained from BASF SE with a loading of $\approx$ 7.7 mg cm^{-2}, corresponding to $\approx$ 1.9 mAh cm^{-2}.

Electrochemical characterization.—Three different cell setups were used: (i) Swagelok T-cells with a Li reference electrode (Li-RE) for determination of the cell-TD-OCV in LMR-NCM/Li half-cells, (LMR-NCM potential measured vs the Li-RE); (ii) coin-cells for electrochemical cycling experiments and recording of the OCV curves; (iii) U-shaped pouch-cells for spatially non-isothermal measurements of the electrode-TD-OCV (see Fig. S1 in the Supporting Information). All cells were assembled in an argon filled glovebox (O_2, $H_2O < 0.1$ ppm, MBraun, Germany).

For Swagelok T-cells, anode and cathode were stacked with two glass fiber separators in between (11 mm diameter, 200 μm thickness, glass microfiber #691, VWR, Germany). The cells were filled with 60 μl of a FEC:DEC (12:64 v:v) based electrolyte with 1 M $LiPF_6$ and 24 vol% of an additional fluorinated co-solvent. The Li-RE (6 mm diameter, 450 μm thickness, 99.9%, Rockwood Lithium, USA) was in electrochemical contact with the cell *via* a separator onto which another 20 μl of electrolyte was added. The 3-electrode T-cell setup is identical to what is described by Solchenbach et al. as the "conventional design".[33] Coin-cells were assembled using a Li counter electrode (16 mm diameter, CE), two glass fiber separators (17 mm diameter) and an LMR-NCM cathode, adding 80 μl of the same electrolyte as was used for the T-cells. The U-cell setup is described in the Experimantal section and in the Supporting Information.

T-cells and coin-cells were cycled at 25 °C (if not stated otherwise) in a temperature-controlled oven (Binder, Germany) using a Biologic potentiostat (VMP300, Biologic, France). At first, one activation cycle at a C-rate of C/15 (2.0–4.8 V, all voltages reported vs Li^+/Li) and two stabilization cycles at C/10 (2.0–4.7 V) were conducted. All C-rates reported here refer to the nominal capacity of the LMR-NCM of 250 mAh g^{-1} (i.e. 1C $\equiv$ 250 mA g^{-1} or $\approx$ 3 mA cm^{-2}). Subsequent to the initial cycles, the electrochemical characterization (OCV curves, determination of the cell-TD-OCV) was carried out at C/10 in the 4th cycle. For measurements at a different C-rate, an additional cycle at that C-rate was done prior to the actual experiment to equilibrate to the new C-rate.

Measurement of the partial molar entropy of the cell.—All measurements were conducted in the 4th cycle subsequent to the initial activation and stabilization procedure explained above. To determine the SOC dependent cell-TD-OCV of LMR-NCM/Li cells, the T-cells were (dis)charged to a certain SOC-point at 25 °C and allowed to relax until the change of the OCV with time was less than $\approx$ 0.2 mV h^{-1}. For each SOC-point, such a relaxation took between 100 h and 200 h. The cells were then transferred to an Espec temperature chamber (LU114, Espec, Japan) to measure the cell-TD-OCV with a defined temperature ramp of 0.5 K min^{-1}. Starting at the initial cell temperature of 25 °C, the temperature ramping commenced with a heating phase to 35 °C. Subsequently, three cycles of cooling to 5 °C and heating to 35 °C were repeated, followed by a final cooling step to the initial 25 °C. Figure 2 shows an exemplary curve of the temperature profile and the respective OCV response. After this measurement sequence, the cell was (dis) charged to the next SOC at 25 °C. This procedure was repeated with several cells in charge and discharge direction to collect data with an SOC spacing of $\approx$ 5% (12.5 mAh g^{-1}). Data treatment was conducted with a Matlab Script determining the slope of the measured OCV data vs time by a linear fitting of the individual ramps. The so derived $\frac{\partial E_0}{\partial t}$ values were averaged and transferred to cell-TD-OCV, $\frac{\partial E_0}{\partial T}$, by allocating them with the predefined temperature ramp ($\frac{\partial T}{\partial t}$). For a detailed discussion on the ramping method, see the Results section. Moreover, the OCV value of the cell at the respective SOC was determined by averaging over the last hour of data points prior to initiating the temperature ramps.

To confirm the accuracy of the data acquired by the Biologic potentiostat, a high sensitivity Nanovoltmeter (Model 2182 A, Keithley Instruments, USA) was used with a Labview Script to record the potential of the cell during temperature variation.

Determination of the Li contribution to the partial molar entropy of the cell.—To accomplish a spatially non-isothermal

environment for the measurement of the electrode-TD-OCV of Li, pouch-cells with a U-shaped geometry were used. A schematic drawing is shown in Fig. S1 in the Supporting Information. For measurements of the electrode-TD-OCV of Li, symmetrical Li/Li U-cells with a Li metal ($\approx$ 1 cm^2, contacted *via* a Ni-tab) at both sides of the cell were used. Electrochemical contact was ensured with a U-shaped glass fiber separator soaked with 2 mL LP57 electrolyte (1 M $LiPF_6$ in EC:EMC = 3:7 by weight, BASF SE, Germany). Using this geometry, the temperature of one Li-electrode was kept constant in a water bath at room temperature while the temperature of the other one was varied between 0 °C and 40 °C using a double-walled glass beaker with an in-, and outlet for cooling fluid connected to a refrigerated-heating circulator (FP50, Julabo, Germany). The temperature at the vicinity of the cell surface of each of the immersed legs of the U-cell was recorded by two USB data loggers (Easylog-USB-2-LCD, Lascar Electronics Ltd, UK). The potential was monitored using the above described Nanovoltmeter. The measurement principle is similar to that described by Swiderska-Mocek et al.[25]

Results and Discussion

Development of an accurate method to determine $\frac{\partial E_0}{\partial T}$.—The partial molar entropy, $\frac{dS}{d\xi}(\xi)$, can be obtained by potentiometric methods *via* determination of the temperature dependence of the OCV (cell-TD-OCV), $\frac{\partial E_0}{\partial T}$, or with calorimetric methods *via* measuring the reversible heat, $\dot{Q}_{rev}$. For calorimetric measurements, however, large cell formats are necessary to reach the required accuracy. In the following, we will focus on the potentiometric method where the TD-OCV is determined by collecting OCV data as a function of temperature. For this purpose, the battery is typically cycled to a certain SOC and allowed to relax in OCV conditions for some time before the temperature of the cell is changed in a step-like procedure.[9,12,34–36] A typical data set for the step procedure is shown in Fig. 1a for a 0.33 LMR-NCM/Li cell at a nominal SOC of 140 mAh g^{-1} in the 4th cycle in charge direction. After 24 h of relaxation at OCV conditions at 25 °C, the temperature of the cell is changed to 35 °C and the cell is given 1 h to accommodate to the new temperature. This is repeated at 25 °C, 15 °C and 5 °C before the temperature is again set to 25 °C. The OCV is thus measured as a direct function of the cell temperature. By making a linear regression of OCV vs temperature (Fig. 1b), the cell-TD-OCV can be determined from the slope. This is repeated at every SOC of interest.

However, there are some challenges when applying this method to determine the TD-OCV. Since the OCV is directly measured as a function of temperature, any relaxation phenomena leading to a change in OCV with time have to be excluded. For the data shown in Fig. 1a, the scatter in the OCV data lead to the error bars in Fig. 1b (standard deviation of calculating the average OCV value during the last 5 min of the respective 1 h temperature step in Fig. 1a). The overall error for the calculation of the cell-TD-OCV hence includes the error from the linear fit and the error of the respective OCV values. For the exemplary data set in Fig. 1, Table I shows that the calculated error is in the same order of magnitude as the resulting

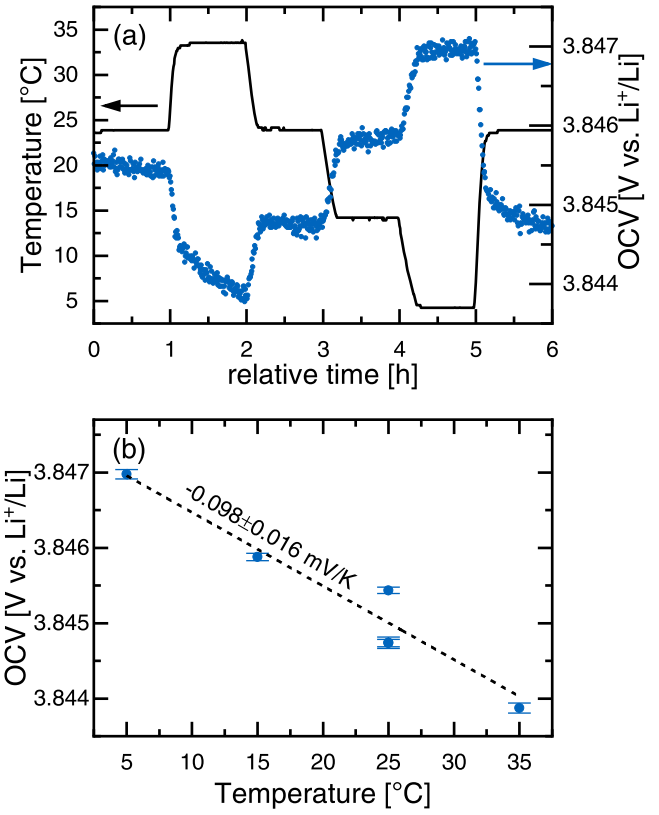

Figure 1. (a) Example of a temperature profile (black line) and the corresponding OCV response (blue symbols) when applying the temperature step method. After equilibrating at OCV conditions for 24 h at 25 °C, the temperature of the battery is varied in steps with a thermal equilibration time of 1 h per step. Here, data from a 0.33 LMR-NCM/Li T-cell at a nominal SOC of 140 mAh g^{-1} during the 4th charge is shown. (b) The cell-TD-OCV is the slope of a linear fit (black dashed line) of the determined OCV values (blue symbols) as a function of the respective temperatures. The error bars of the OCV data are the standard deviation calculated from averaging over the last 5 min of every 1 h temperature step. The error of the resulting cell-TD-OCV includes the error from the linear fitting and the errors of the data points.

TD-OCV value after 24 h of relaxation. Voltage relaxation processes cannot be fully avoided and are reported to take up to six months depending on the cell chemistry.[37] However, a survey of entropy studies by Zhang et al.[22] showed that typically waiting times of 3 h and 60 h were provided for voltage relaxation at each SOC point. Figure 1a serves to illustrate that a relaxation time of 24 h is not sufficient (for this cell chemistry, at this SOC) since ongoing voltage relaxation is observable, which is especially pronounced at higher temperatures. This leads to the fact that three different OCV values are determined at 25 °C during the step method. On the other hand, during prolonged relaxation periods, self-discharging phenomena within the battery have to be taken into account. Especially at high

Table I. Cell-TD-OCV of a 0.33 LMR-NCM/Li cell determined at an SOC of 140 mAh g^{-1} during the 4th charge after 24 h and 96 h of relaxation in OCV conditions at 25 °C. Results from the step method and ramp method are contrasted (by comparing data from two identical cells). The difference between the absolute results after 96 h from the two different methods is caused by cell to cell variations. For the step method, the error is calculated from the fit through the OCV data as a function of temperature including the error from the OCV determination. For the ramp method, the error results from averaging over six dE/dt values including their respective error from the linear fitting of the ramps.

Equilibration time [h]	Cell TD-OCV [mV K^{-1}] with error in parenthesis	
	Step method	Ramp method
24	−0.098 (0.016)	−0.127 (0.002)
96	−0.115 (0.006)	−0.123 (0.001)

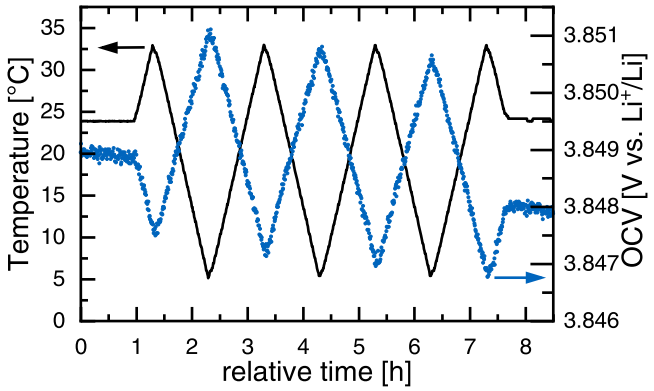

Figure 2. Typical OCV profile during the application of the linear temperature ramp method where the temperature is varied linearly between 5 °C and 35 °C with a rate of 0.5 K min^{-1} (black line) while the OCV is recorded (blue symbols). Here, data from a 0.33 LMR-NCM/Li T-cell at a nominal SOC of 140 mAh g^{-1} during the 4th charge is shown after equilibrating the cell at OCV conditions for 24 h at 25 °C.

SOCs, it may become difficult to maintain a stable voltage.[12,35,38] Figure S2 in the Supporting Information exemplarily shows that a pronounced voltage relaxation at a high SOC considerably compromises the determination of the TD-OCV with the step method. To circumvent extended waiting times, Osswald et al.[39] suggested to extrapolate the stationary state voltage by fitting the truncated relaxation curve. By correcting for self-discharge[35] or by short charge/discharge phases at low currents,[40] attempts have been made to minimize the effects of self-discharging and parasitic side reactions. Another issue was identified by Zilberman et al.,[37] who found a temperature path dependent voltage behavior causing uncertainties in the determination of the true OCV values. Therefore, they suggested to limit the temperature amplitude and the thermal equilibration time, and use both cooling and heating temperature variations to determine accurate TD-OCVs.[37] Usually, a temperature range between 20 °C and 30 °C is applied,[22,39,40] though some researchers use wider ranges (from 0 °C up to 55 °C) for a better signal-to-noise ratio.[22,34,35] Of course, also appropriate measurements of the cell temperature are required for valid TD-OCV data. In summary, the step procedure, although widely used in the literature, faces some issues, pertaining to the accurate determination of an OCV value per temperature step.

To overcome these difficulties, we applied a linear temperature ramp method, which is less common in the field and was only used by a few other research groups before.[16–18] This is why we want to discuss it in more detail. The here used temperature profile is similar to what was applied by Thomas et al.[40] and an exemplary data set of our ramp method is shown in Fig. 2. The temperature was varied linearly between 5 °C and 35 °C at a rate of 0.5 K min^{-1}. By doing so, the OCV is measured on the fly while the temperature is continuously changed, in contrast to the above discussed classical temperature step technique. Since the OCV is a linear function of the temperature (within a reasonable temperature range), the slope of the OCV change follows the linearity of the applied temperature profile. With the knowledge of the rate (e.g. $\frac{\partial T}{\partial t} = 0.5$ K min^{-1}), the slope of the OCV ($\frac{\partial E_0}{\partial t}$ in mV h^{-1}) is easily converted to the TD-OCV ($\frac{\partial E_0}{\partial T}$ in mV K^{-1}). Figure 2 shows that the effective temperature range, which was monitored by a temperature sensor close to the cell surface, is slightly smaller ($\approx$ 5 °C–33.5 °C) than what is given by the thermostat (5 °C–35 °C). This might be related to the accuracy of the temperature chamber and the temperature sensor used. To find an optimum temperature range, a compromise has to be reached between two requirements: A large temperature range is desirable to get as much data as possible. For the cell chemistry, the temperature range should be restricted to reasonable limits to avoid side reactions. This is why the range between 5 °C and 35 °C was chosen.

To validate the results from the temperature ramp method, the cell-TD-OCV was first determined *via* the temperature step procedure and then compared to that determined by consecutive temperature ramp procedures with rates of 0.5 K min^{-1} and 1 K min^{-1}. For this experiment, a cell was charged to a certain SOC, allowed to relax at OCV for $\approx$ 60–150 h (until the change in OCV was less than $\approx$ 0.2 mV K^{-1}), and then the temperature was first changed according to the step profile and then according to the two ramp profiles. The results are shown in the Supporting Information in Fig. S4 and confirm that the temperature ramp method gives the same results as the temperature step method. Minor deviations may arise from the differences in calculating $\frac{\partial E_0}{\partial T}$ between the temperature ramp and the step method (see discussion of the data accuracy below), but are negligible with respect to other sources of errors (e.g. accurate determination of the SOC, cell to cell variations). Furthermore, it is proved that the results from the ramp method are independent of the applied rate (as long as a reasonably slow rate is applied). A detailed analysis of the temperature ramp data sets shows that the potential change is delayed with respect to the applied temperature change by about 2 to 5 min (see Fig. 2), which gives an idea about the thermal conductivity of the cell. Due to this deviation from the ideal triangular behavior, the OCV data at the boundaries of each ramp were not included into the linear fit (approx. the first and last 5 min of each 60 minute ramp, effectively reducing the analyzed temperature window to $\approx$ 8 °C–30 °C). Since the voltage responses of interest have rather small absolute values, we validated the accuracy of the data obtained from the Biologic potentiostat (resolution of $\approx$ 100 μV) with a high precision Nanovoltmeter (resolution of $\approx$ 1 μV in the mode used here). As a quality criterion, the residual sum of squares of linear fits of the obtained triangle wave data is used. For the data measured by the Nanovoltmeter (not shown here), this parameter is four orders of magnitude below the one for the Biologic, suggesting a significantly lower noise level. However, both data sets give very similar results for $\frac{\partial E_0}{\partial T}$ (differing by less than $\approx$ 0.01 mV K^{-1}). Since the data from the Biologic show only white noise, which is significantly smaller than the actual signal intensity (see Figs. 1 and 2), and since the results are practically the same as those obtained from the Nanovoltmeter, all further measurements were conducted with the Biologic potentiostat.

In the following, the temperature step and ramp method will be compared. Figure 2 shows data collected during a temperature ramp experiment with an identical cell as used for the temperature step method in Fig. 1 (both at 140 mAh g^{-1} during the 4th charge after 24 h of relaxation at 25 °C). For the temperature ramp method, the TD-OCV is calculated based on the slope of the triangular OCV data. The error therefore includes the error of the linear fit of the respective ramps and the error from taking the average over six values. Table I shows that for the ramp method, the calculated error is one order of magnitude smaller compared to the error resulting from the step method. Both measurements were repeated after 96 h of relaxation, when the change of the OCV with time was sufficiently low (<0.1 mV h^{-1}) to allow for a reliable determination of the TD-OCV. In case of the temperature ramp method, the result obtained after 24 h of relaxation is very close to the TD-OCV value determined after 96 h of relaxation. For the step method, however, the deviation between the two TD-OCV values is relatively large. This illustrates that the temperature ramp method is less sensitive to ongoing voltage relaxation compared to the step procedure. This is achieved by applying several heating and cooling ramps, which result in triangular OCV response curves with positive and negative slopes, so that any effects resulting from incomplete OCV relaxation are minimized. This is furthermore illustrated in Fig. S3 in the Supporting Information, where an ongoing relaxation at a high SOC leads to a gradual decrease of the OCV over time. The relaxation effect has an opposing sign, thus a weakening effect on the OCV

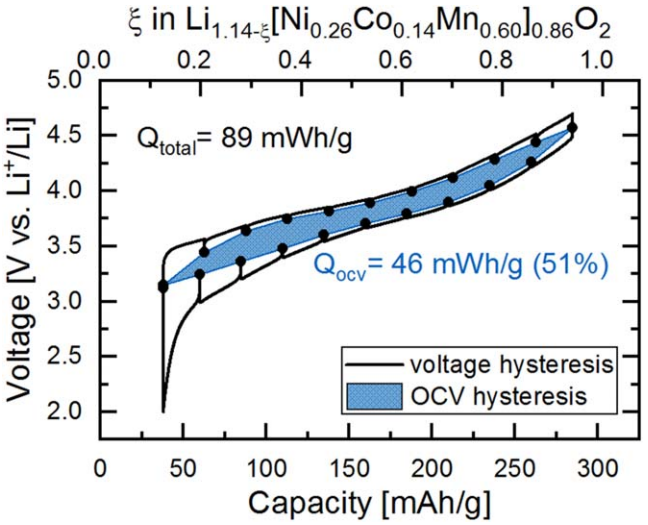

Figure 3. Voltage hysteresis at C/10 (25 °C) in a 0.33 LMR-NCM/Li cell shown vs specific capacity (lower *x*-axis) and extent of reaction (upper *x*-axis). The black line is the voltage curve at C/10 with intermittent 1 h OCV phases every ≈ 10% SOC (i.e. every 25 mAh g^{-1}), leading to the black circles. The total voltage hysteresis amounts to 89 mWh g^{-1} (area enclosed by the black line) and the OCV hysteresis at zero current equals 46 mWh g^{-1} (blue area, enclosed by OCV points, amounting to 51% of the total area).

behavior during cooling and an amplifying effect during heating. By measuring both temperature pathways multiple times and averaging over the acquired slopes, any error due to OCV relaxation is minimized. This also means that even if the OCV is not perfectly stable, the entropy data obtained with the temperature ramp method are reliable. If sufficiently long relaxation times are applied, the advantage of the temperature ramp method is less pronounced. Table I shows that after 96 h of relaxation, the calculated errors of the TD-OCV of both methods are similar. We want to stress, however, that prolonged relaxation times can lead to self-discharge phenomena (especially at high SOCs), which might again cause a pronounced change of the OCV with time. For these cases, the temperature ramp method is more suitable than the step procedure. The difference between the two final $\frac{\partial E_0}{\partial T}$ values might arise from minor deviations in the determination of the SOC for the two different cells and from cell to cell variations. The measurement was repeated after 220 h of relaxation and the respective TD-OCV values of both cells did not change significantly. The errors from the calculation are thus relatively small in comparison to experimental errors.

Although effects from voltage relaxation are minimized by the temperature ramp method, the cells of this study were allowed to rest at each SOC until the change in OCV was on the order of ≈ 0.2 mV h^{-1}, leading to relaxation times of 100–200 h per SOC step. Of course, such extended OCV periods, especially at high SOCs, cause self-discharge and lead to an inaccuracy in the determination of the SOC. To avoid accumulated self-discharge during repeated, prolonged observation intervals using a single cell, a number of identical cells was used instead to measure the TD-OCV at given SOC points during charge and discharge, with every cell undergoing only three to five measurements. All OCV values determined prior to the temperature ramp method, were in good agreement with the nominal OCV curve (see Fig. 3). The use of a set of cells for these measurements not only increased the accuracy of the SOC determination, but also helped to speed up the collection of a complete entropy data set for a whole charge/discharge cycle significantly. Additionally, with the use of multiple cells, the reproducibility of the results could be verified by measuring at nominally identical SOC points. Small cell to cell variations were observable, which however were negligible within the limits of accuracy of the measurements.

Li electrode contribution to the partial molar entropy of LMR-NCM/Li cells.—As was explained in the Theoretical Considerations above, we aimed at clarifying the contribution of Li to the cell entropy by spatially non-isothermal measurements using custom-made U-shaped pouch cells (Figure S1 in the Supporting Information). In this setup, one side of the U-cell is exposed to temperature changes induced by a water bath, while the other side is held at a constant temperature, similar to the approach reported by Swiderska-Mocek.[25] In symmetrical Li/Li U-cells, the electrode-TD-OCV of Li was directly determined. When both electrode compartments are at the same temperature, the OCV is zero. As soon as the temperature of one side deviates from the other one, the potential changes. By measuring the OCV as a function of this temperature difference, the electrode-TD-OCV of Li can be determined. The average over multiple measurements with a number of different cells gives $\{\frac{\partial E_0}{\partial T}\}_{Li} = 1.12(\pm 0.06)$ mV K^{-1}. We found that the results are independent of whether a fresh piece of Li metal was used or one harvested from a cycled LMR-NCM/Li cell. This means that the contribution of Li to the cell TD-OCV is independent of the cycling history and nominal SOC of the Li, which is in agreement with literature reports.[19,20] An exemplary data set of such a measurement is shown in Fig. S5 in the Supporting Information. However, as mentioned above in the theory section, this value includes the Soret effect, since in the spatially non-isothermal setup, thermodiffusion is present (see Eq. 15). A comparison to literature reports shows that Huang et al.[41] have done a similar experiment with a cell consisting of two single-electrode tubes containing identical Li electrodes that are connected by an electrolyte filled plastic tube. The electrode tubes were placed in two oil-bath systems at different temperatures. With the above discussed temperature stepping method, they obtained a value of 1.17 mV K^{-1},[41] which is in good agreement with our result. As in the case of our U-cell experiment, their approach also includes the Soret effect. However, they have complemented their experiments with an electrochemical-calorimetric measurement where one Li electrode is inside the calorimeter and one outside. By cycling with small currents and subtracting the discharge from the charge heat, the irreversible heat is removed and the reversible heat can be determined. From that, they calculate the so-called "entropy of the Li single electrode reaction" to be 128.3 J (mol K^{-1}).[41] Using Eq. 10, this value converts to an electrode-TD-OCV of 1.33 mV K^{-1}. Since there is no Soret effect present in their calorimetric measurement, the difference between their potentiometric value of 1.17 mV K^{-1} and their calorimetry derived value of 1.33 mV K^{-1}, equating to −0.16 mV K^{-1}, would correspond to $\left\{\frac{\partial E}{\partial T}\right\}_{Soret}$ (based on Eq. 15 and assuming $\left\{\frac{\partial E}{\partial T}\right\}_{Seebeck}$ to be negligible). It should be noted that other measurement errors like the inaccuracy of the calorimeter might be affecting the result. Also, charge-neutral exothermic side reactions can contribute to the calorimetric signal and hence lead to an overestimation of the electrode-TD-OCV. The observed difference between the two reported values is therefore only a rough estimate for the contribution of the Soret effect. We can therefore conclude that the Soret effect is negligible in comparison to our $\left\{\frac{\partial E_0}{\partial T}\right\}_{Li}$ value of 1.12(±0.06) mV K^{-1} and that our result agrees with the values reported in the literature.[25,41] According to Eq. 10, a $\left\{\frac{\partial E}{\partial T}\right\}_{Li}$ value of 1.12 mV K^{-1} converts to a molar entropy of 108 J (mol K^{-1}) for Li. We want to stress that this value cannot directly be compared to the textbook value of 29 J (mol K^{-1})[42] since the latter refers the entropy of formation of Li metal at standard conditions while we measure the molar entropy change for depositing Li at the metal anode and the entropy of desolvation of Li^+ ions (see Eq. 5).

From similar spatially non-isothermal measurements with LMR-NCM electrodes, we determined the electrode-TD-OCV of LMR-NCM at certain SOC points (data not shown here). We found that the contribution of Li to the cell-TD-OCV of the LMR-NCM/Li cell is in the same order of magnitude as the one of the LMR–NCM

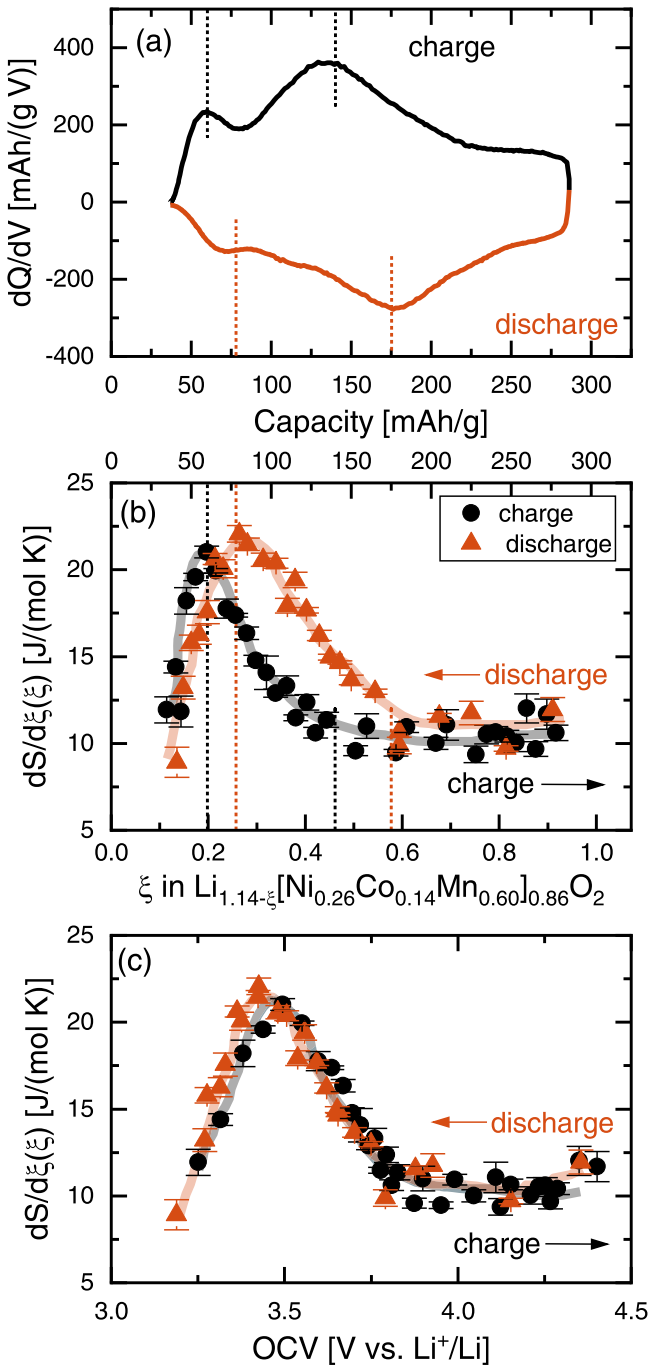

Figure 4. (a) dQ/dV vs capacity plot of a 0.33 LMR-NCM/Li cell recorded at C/10 (25 °C) in the 4th cycle. (b) Partial molar entropy for 0.33 LMR-NCM/Li cells obtained from cell-TD-OCV measurements using the temperature ramp procedure during charge (black circles) and discharge (orange triangles) in the 4th cycle as a function of capacity (upper *x*-axis) or reaction turn-over ξ (lower *x*-axis). (c) Same partial molar entropy data but plotted as function of OCV. Trendlines are shown as guide for the eye. The error bars are calculated mean standard deviations from the calculation of TD-OCV values. Dashed lines highlight common features in the different plots.

cathode (both on the order of ≈ 1 mV K^{-1}), and only the difference of both gives the observable small values around ≈ -0.1 mV K^{-1} for the cell-TD-OCV. Swiderska-Mocek et al.[25] also report such high electrode-TD-OCV values for the CAMs used in their study.

Conclusively, the entropy contribution of Li as a counter electrode must not be assumed to be zero but has to be treated as an SOC-independent offset value. It is important to keep in mind that any counter electrode will contribute to the measured entropy curve, even if the contribution is only an offset, as for Li. This is especially crucial when discussing an apparent change in the sign of the $\frac{dS}{d\xi}(\xi)$ curve, which, in the literature, is often solely ascribed to processes in the cathode active material.[22,40] Such a hypothesis is not valid for the data presented here and any suppositions presented elsewhere need to be revisited.

Hysteresis phenomena in LMR-NCM cathode active materials.—The active material of interest in this study is Li-, and Mn-rich NCM and the main focus is on the material 0.33 LMR-NCM ($Li_{1.14}[Ni_{0.26}Co_{0.14}Mn_{0.6}]_{0.86}O_2$). LMR-NCM exhibits characteristic hysteresis phenomena, which are extensively discussed in the literature. In general, a hysteretic behavior occurs if sufficiently high energy barriers prevent an equilibration between stoichiometrically equivalent states located along energetically different charging and discharging pathways. In this case, changes in state will occur via thermodynamically metastable regions.[43] The resulting hysteresis loop as a whole is unidirectional but reversibility may hold within limited path sections. The most striking of these phenomena in LMR-NCM is the OCV hysteresis, which is shown in Fig. 3 (blue shaded area). The overall voltage hysteresis can be separated into two parts, (i) a voltage hysteresis due to charge transfer and concentration overpotentials, which is common for all types of active materials, scaling with the applied current and being zero at open circuit conditions, and (ii) the OCV hysteresis, which is independent of the applied current (see Fig. S6 in the SI and discussion below) and is hence a material specific property. At a low C-rate as C/10, the energy loss caused by the OCV hysteresis loop (represented by the blue shaded area in Fig. 3) can amount to 51% of the total voltage hysteresis loop (represented by the area that is enclosed by the black line).

Several reasons for the OCV hysteresis in LMR-NCM are discussed in the literature, mainly focusing on reversible transition metal migration[44] and changes of oxygen redox,[45] causing the re-entrant Li environment during discharge to be energetically different from that during charge.[4,46] The phenomenon of hysteresis in LMR-NCM is not only observable in the voltage curve, but also in a path dependent cathode resistance[1–3] as well as in the SOC dependent hysteresis of LMR-NCM lattice parameters[5,6] and atomic distances.[7] The OCV hysteresis is of particular interest for this study, because it directly reflects the chemical potential, constituting a basic thermodynamic property. This is why we investigated the influence of different factors on the OCV hysteresis of LMR-NCM. For the analysis of the effect of the C-rate, we applied a special cycling protocol. Since the width of the SOC window in a voltage-limited cycling procedure depends on the applied current (and the resulting overpotential), a comparison of the overall energy associated with the OCV hysteresis (integration of the OCV hysteresis loop) at different C-rates is not directly possible. However, by using a cycling procedure that is controlled by specific capacity cutoffs (i.e. limiting the overall SOC window), the comparison of the OCV hysteresis obtained at different C-rates becomes possible. Figure S6 in the SI compares the OCV curves at 1C, C/2, and C/10, revealing a perfect overlap of the OCV hysteresis loops. Thus, the OCV hysteresis is independent of the applied current. This observation indicates that there is a static barrier causing the hysteresis, which is not subject to the dynamics of charging/discharging. Another influencing factor that was investigated is the temperature. To investigate the temperature dependence of the OCV hysteresis, OCV data were collected at 0 °C and 45 °C in a capacity limited cycling procedure. The resulting data are shown in Fig. S7 in the SI. The OCV hysteresis is larger at higher temperature, which is in agreement with literature reports on LMR-NCM.[47] Processes, which are kinetically hindered, are expected to accelerate with increasing temperature. It seems, however, that the energetic barriers leading to the OCV hysteresis in LMR-NCM cannot be overcome at the temperature of 45 °C. It is conceivable that the temperature

necessary to eliminate the OCV hysteresis is beyond the operating temperature of a battery and might even be beyond the thermal stability of the CAM.

Another factor affecting the OCV hysteresis is the degree of overlithiation of the LMR-NCM material. A higher degree of overlithiation leads to an increase of the OCV hysteresis loop. This will be discussed in more detail with regards to Fig. 6. The following entropy measurements are intended to investigate possible interrelations between entropy and hysteresis phenomena in LMR-NCM and to open a new perspective on the current discussion in literature.

Partial molar entropy of LMR-NCM.— *Path dependence of the partial molar entropy of LMR-NCM.*—By applying the temperature ramp method, cell-TD-OCVs of 0.33 LMR-NCM vs a Li-RE were acquired during charge and discharge at every ≈ 5% SOC. In Fig. 4b, the resulting partial molar entropy, $\frac{dS}{d\xi}(\xi)$, is depicted as a function of SOC. During charge (black circles), the entropy curve shows a distinct peak at $\xi \approx 0.20$ and a plateau-like behavior above $\xi \approx 0.50$. Upon discharge (orange triangles), this plateau only extends down to $\xi \approx 0.58$, where a similar peak begins to evolve. Its maximum at $\xi \approx 0.26$ is significantly shifted as compared to the charge direction. As discussed above, any effects of self-discharge are minimized by the temperature ramp method and the SOC values are verified by comparing the OCV values collected after 1 h (Fig. 3) to that after extended waiting times (entropy measurements). Therefore we are confident that the observed shift of the partial molar entropy curve along the ξ axis during charge and discharge is relevant.

If however, $\frac{dS}{d\xi}(\xi)$ is plotted vs the OCV, this shift of the partial molar entropy peak vanishes, as can be seen in Fig. 4c. In this case, both peaks exhibit the same shape and coincide with each other. This important finding shows that the OCV, and not ξ, is a unique descriptor of the thermodynamic changes being responsible for the entropy change occurring at the observed peak. The same observation is reported for the lattice parameters in LMR-NCM, revealing a hysteresis when plotted as function of SOC, which, likewise, vanishes when plotted as a function of OCV.[6] Since the OCV essentially mirrors the change of the Gibbs free energy of the LMR-NCM, these findings demonstrate that OCV, entropy and Gibbs free energy all experience a pronounced hysteresis while they remain thermodynamically correlated among each other.

Our entropy curves differ in shape from those of Shi et al.[48] who also investigated the entropy of Li- and Mn-rich cathodes with the classical temperature stepping method, however, using a rather short relaxation phase (90 min) and short-time temperature steps (15 min). It remains unclear, how far the differences to our data result from the use of a different LMR-NCM material or whether it is due to their very short OCV equilibration times, which we would consider far too short to yield reliable TD-OCV data. The magnitude of the entropy values of LMR-NCM is fairly comparable with the data for regular layered oxides.[20,35,49]

Another interesting finding is that distinct features of the $\frac{dS}{d\xi}(\xi)$ curve vs SOC correlate well with peaks in the dQ/dV plot recorded at the same rate but without intermittent OCV periods (see Fig. 4a), as marked by the dashed lines in Figs. 4a and 4b. Schlueter at al.,[13] also report a correlation between peaks in the dQ/dV plots of $LiMn_2O_4$ and features in the respective entropy profile. In charge direction, the position of the maximum of the entropy peak at $\xi \approx 0.20$ coincides with the location of a peak in the dQ/dV plot (see leftmost set of black dashed lines). This dQ/dV peak is usually assigned to the $Mn^{3+/4+}$ redox reaction.[50] Another peak in the dQ/dV plot during charge is observed where the entropy curve starts the plateau (near $\xi \approx 0.50$; marked by the second set of vertical black dashed lines). It is mainly assigned to $Ni^{2+/3+/4+}$ and $Co^{3+/4+}$ redox chemistry.[50] In the discharge direction, the same correspondence between the peaks in the dQ/dV vs capacity plot and the partial molar entropy vs capacity plot is observed (marked by the vertical orange dashed lines). Since these redox reactions are guided by the Gibbs free energy, it is not surprising that the dQ/dV plot shows the same hysteresis as a function of SOC, as the OCV and the entropy curve.

Discussion of the configurational entropy.—The configurational entropy can be represented by a statistical distributional model of Li on available lattice sites. In the literature, two structural models are typically used to explain common features in entropy curves. One refers to an ideal solid solution, where all vacancies in the lattice are filled randomly.[14,15] The other model is based on two or more energetically different sub-lattices, which are filled in energetic order.[13–15] The entropy curves of LMR-NCM/Li, however, show none of the typical fingerprints of those configurational entropy profiles. There are several reasons why configurational entropy is not expected to be dominating the $\frac{\partial S}{\partial \xi}(\xi)$ curve in case of LMR-NCM/Li, which will be discussed in the following.

Configurational entropy should in principle always be a function of the distributional variability of Li in the CAM, hence the SOC of the cell. Because of the steep voltage curves of LMR-NCM/Li ($\frac{\partial U}{\partial x} \approx 1.5$ eV), the amount of thermally exchangeable Li sites near the Fermi level is very small ($\Delta x_{exchange} = \frac{RT}{F \bullet \frac{\partial U}{\partial x}} = 1.7\%$). We do therefore not expect any significant contributions from the configurational entropy in our system. Another important consideration is the fact that there is a path dependence of $\frac{\partial S}{\partial \xi}(\xi)$ vs SOC, which vanishes as a function of OCV. This means that the entropy is a function of the OCV (= chemical potential of the LMR-NCM) and not directly of the amount of Li in the structure, which we would expect in case of a dominating configurational entropy. The broadness of the peak in the $\frac{\partial S}{\partial \xi}(\xi)$ curve can be explained by a continuous modification of the LMR-NCM structure during (de-)lithiation, which is proven by XRD measurements.[5,6] The ongoing change in the chemical potential of lithium entering the host lattice during discharge (and leaving the CAM during charge) might lead to a smearing out of any contributions from configurational entropy in contrast to the situation of an ideal solid solution where all Li sites are energetically equal leading to distinct curve features from configurational entropy. Another reason why the contribution from the configurational entropy might not be visible is that the overlithiation of the LMR-NCM and hence the removal of Li from the transition metal layer might lead to the formation of domains with only a limited amount of Li vacancies. This would effectively suppress the distributional variability of Li ions over the host lattice and reduce the configurational entropy of the whole structure. In support of this argument, it was reported in the literature that the overlithiation of $LiCoO_2$[51] and $Li_2Mn_2O_4$[13,14] reduces the characteristic features of the configurational entropy by the formation of pinned Li in the host structure.

Discussion of the vibrational entropy.—The vibrational entropy was introduced in theory section above and was reported to give a constant offset.[20] In the case of LMR-NCM, where we observe a hysteretic behavior and a lack of typical fingerprints of configurational entropy, it is worth to discuss the possible influence of the vibrational entropy. Heubner et al.,[52] who also observed a peak in the entropy profile of their active material $NaFePO_4$ followed by a flat behavior with increasing SOC, speculated that contributions from vibrational entropy are possible. For LMR-NCM, owing to the low mass of Li, any confined movement within the Li layer should lead to rather high frequency vibrations and is thus not expected to be active at ambient temperature. Therefore, any change of vibrational entropy in the LMR-NCM must be caused by the host lattice itself. It is conceivable that low-frequency translational vibronic

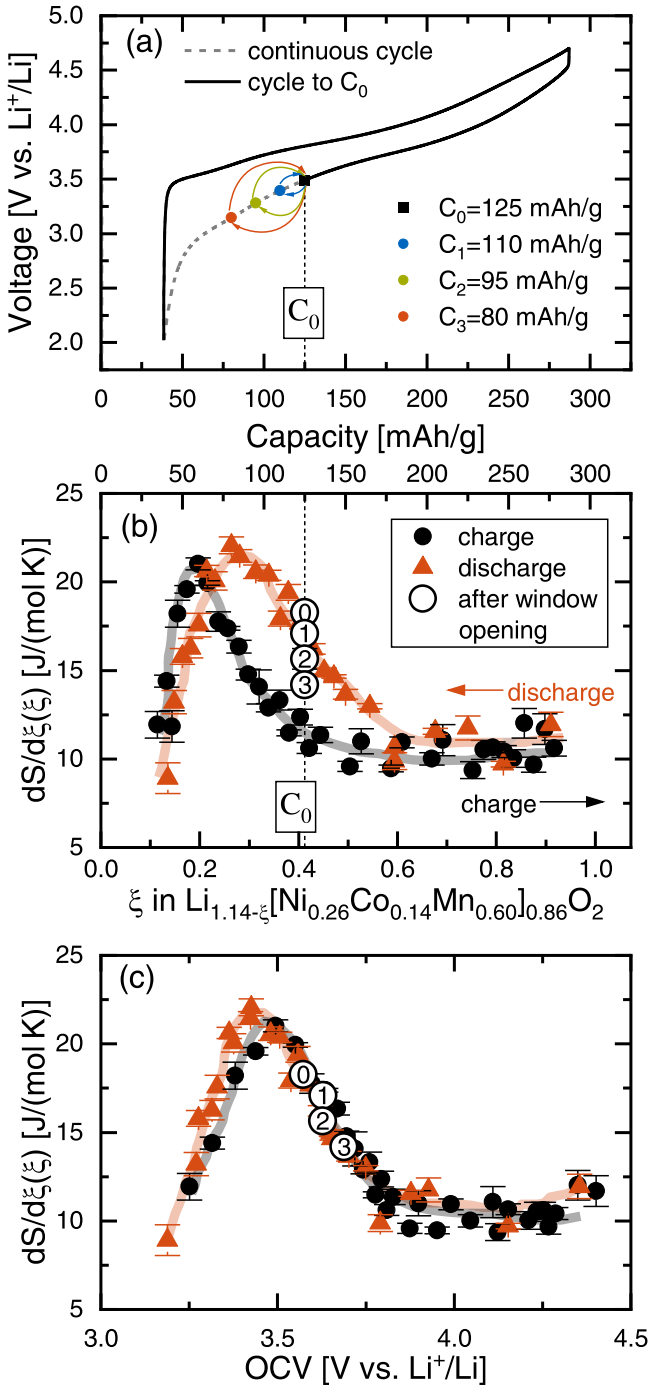

Figure 5. Results from window-opening experiments in discharge direction for 0.33 LMR-NCM/Li cells after activation/stabilization. (a) The voltage curve for the 4th cycle with a continuous cycle indicated by the gray dashed line and the charge/discharge procedure prior to the window-opening marked by the black line. The window-opening loops from the reference point C_0 to the turning points C_1-C_3 are indicated by colored arrows; (b) partial molar entropy during charge (black circles, same data as in Fig. 4) and discharge (orange triangles, same data as in Fig. 4) with trendlines as a function of capacity (upper *x*-axis) or reaction turnover (lower x-axis); (c) same data as a function of OCV. Measurement procedure: (i) after activation/stabilization, cells were charged to 4.7 V and discharged to an absolute capacity of 125 mAh g^{-1} (C_0) at C/10 and 25 °C; (ii) subsequently, cells were discharged to either $C_1 = 110$ mAh g^{-1}, $C_2 = 95$ mAh g^{-1} or $C_3 = 85$ mAh g^{-1} and then charged again to C_0 (all at C/10 and 25 °C); (iii) at C_0, the cells were allowed to rest until the change in OCV was less than ≈ 0.2 mV h^{-1}, after which the cell-TD-OCV was determined. The resulting partial molar entropy data points from the window-opening are labeled according to their maximum discharge capacity window (C_0≡⓪, C_1≡①, C_2≡②, C_3≡③).

modes of the host lattice will be disturbed or suppressed by the presence of Li ions. Possible scenarios are disruptions of vibrations by dislocations of lattice chains, which can be caused by Li (de-) intercalation and its influence on the interlayer distance, transition metal migration, and the formation of clusters. Another reason is a change in the stiffness[53] of the host lattice, e.g. by oxidation/reduction of the transition metals or by oxygen redox. In any case, the vibrational entropy is expected to be a function of the energetic state and structure of the host lattice. From XRD studies, it is already known that the LMR-NCM structure changes as a function of OCV and shows a hysteresis as a function of SOC[5,6]—similar to what is observed for the partial molar entropy. This is why it is reasonable to assume that the entropy profile of LMR-NCM is dominated by changes in the vibrational entropy of the host lattice (expected to be a function of OCV) rather than configurational entropy of the Li atoms in the structure (expected to be a function of SOC).

Typically, a peak in the $\frac{\partial S}{\partial \xi}(\xi)$ profile is correlated to a phase transition.[54,55] For example, McKinnon et al.[56] found a broad peak in the entropy profile of $Li_xMo_6Se_8$ around x = 2.8, which they ascribed to the phase transition between the triclinic and the rhombohedral state. They also report a peak in the dQ/dV at the same SOC. Interestingly, they also observe a shift of the peak between charge and discharge direction, translating to a shift in the respective phase boundaries. A broad peak as observed for LMR-NCM is typically ascribed to a second order phase transition. Any phase transition in the electrode should be driven by the chemical potential and should therefore correlate with the OCV, as is the case here. It is therefore conceivable that at an OCV of $\approx$ 3.5 V (Fig. 4c), the LMR-NCM is transformed in a way that gives rise to the observable peak in the entropy profile. However, it needs to be stressed that what we propose here is no structural phase transition in terms of two crystallographically different symmetries, for which diffraction studies clearly give no evidence.[5,6] We rather assume an energetic difference between the two phases, similar to what was proposed by Assat et al.[57] The description of the LMR-NCM structure in terms of energetically different domains was already discussed in the context with impedance measurements, where an asymmetry between the area-specific impedance of LMR-NCM during charge and discharge and an anomalous rise at low SOCs during discharge is observed.[1–3] This path dependence of the impedance shows some similarity with the entropy shown in Fig. 4. Chen et al.[2] ascribe this phenomenon to bulk rather than interfacial processes within LMR-NCM. They propose that the activated LMR-NCM can be viewed by a percolating network of layered-type, ordered domains with facile Li diffusion, interspersed with disordered domains, which have significantly higher barriers for Li diffusion. Once the layered sites are filled upon discharge, mostly sites in disordered domains remain that represent a considerable barrier for Li diffusion and cause the observable rise in the impedance. Gowda et al.[3] follow a similar line of argumentation by describing the LMR-NCM as a nano-composite of Ni- and Co-rich domains with facile Li diffusion and Li- and Mn-rich domains with sluggish Li diffusion. At this point, we want to make clear that we differentiate between the "phase transition" itself and the process causing its path dependence (and the other hysteresis phenomena) as a function of SOC.

Window-opening experiments.—Before we discuss the window-opening experiments, we will briefly summarize the definitions to describe hysteretic phenomena, as for instance summarized by Neumann.[43] Hysteresis loops indicate process pathways along thermodynamically metastable states, which are separated by energy barriers from lower equilibrium states. Referring to the CAM in our study, these can in the simplest case originate from interactions between Li ions but may also involve more complicated interactions with the host lattice, for example via charge compensating redox mechanisms. In the latter case, cooperative effects, including domain-like structures, may effectively hinder transitions to the

equilibrium state. Such high energy barriers can be overcome, however, by supplying external energy (e.g. by charging/discharging) whereby the system reaches regions with lower barriers via metastable pathways. There, a relaxation to the more stable state finally occurs, which, if it is sufficiently exothermic, is unidirectional and quasi irreversible. If the process is reversed (e.g. on discharge), the system will return to the initial state along a different metastable pathway, which eventually crosses the initial path. Here again, energy barriers will prevent immediate joining with the initial pathway before the barrier becomes small enough for the backwards relaxation. When the associated interaction domains are not uniform, e.g. because of size or local composition, the energies and barriers contributing to the overall hysteresis pathways will vary accordingly. Then, transitions between both hysteresis branches will not occur uniformly but will be spread throughout the hysteresis loop, which will be a composite of a distribution of individual hysteresis loops. These can be explored with so-called scanning curves, which can give insights into the arrangement of the energy barriers. As long as external perturbations are restricted to regions of metastability, the behavior of a domain is apparently reversible but as soon as the external changes proceed beyond the point, at which the energy barriers can be overcome, a relaxation occurs, which causes the domain to remain in the new stable state even if the original external conditions are re-established. It needs to be stressed here, that when we use the words "equilibration" or "domain" we do not refer to actual crystallographic phase changes and domains (for which there is no evidence), but rather use the general concept of hysteresis and apply it to the situation in LMR-NCM cathode active materials. Thereby, "equilibration" describes all changes in the LMR-NCM phase upon (de-)lithiation (e.g. structural, energetic, ordering, etc.) and 'domain' characterizes a structural unit or region in the LMR-NCM (e.g. primary particles, individual crystallites, etc.), which is considered homogeneous, meaning that its elemental units change their state cooperatively.

For 0.33 LMR-NCM/Li cells, the analysis of scanning curves within the hysteresis loop is done by conducting so-called window-opening experiments, in which starting from a certain SOC point, the charge (or discharge) SOC window is sequentially opened. Croy and co-workers have already found a gradual opening of the OCV hysteresis loop for LMR-NCM materials when conducting window-opening experiments.[44,58] In a similar manner, we investigated the path dependence of the entropy in the discharge branch of the hysteresis. As shown in Fig. 5a, this was accomplished by the following protocol: After the activation and two stabilization cycles (not shown), another C/10 charge up to 4.7 V was conducted, followed by a C/10 discharge (black line) to an absolute capacity of $C_0 = 125$ mAh g^{-1} (black symbol). After relaxation in OCV (until the change in OCV was less than ≈ 0.2 mV h^{-1}), the TD-OCV was measured at this reference point. It is marked with a ⓪ in Figs. 5b and 5c. Starting from the reference capacity C_0, discharge-charge loops (window-opening loops, indicated by the colored arrows in Fig. 5a) were conducted with identical cells. After the respective turning points (marked by colored symbols in Fig. 5a) at absolute capacity values of $C_1 = 110$ mAh g^{-1} (blue), $C_2 = 95$ mAh g^{-1} (green), $C_3 = 80$ mAh g^{-1} (orange), the cells were again charged back to C_0 (without any OCV phase in between). There, the cells were allowed to rest in OCV until the change in OCV was less than ≈ 0.2 mV h^{-1}, before the TD-OCV was measured after each window cycle at the same C_0 and compared to that measured during a normal discharge (data point ⓪, without previous discharge/charge loops).

Figures 5b and 5c show the entropy data from the window-opening experiment together with the partial molar entropy curves from Fig. 4. When the SOC window is only opened up to point C_1, the entropy measured at the reference point C_0 has not changed (data point marked by ①). However, if the SOC window is opened further to point C_2 and C_3, the entropy measured at C_0 increases and moves towards the entropy curve for charge (② and ③ in Fig. 5b. At the same time, the respective OCV increases as shown in Fig. 5c. Thus, the relaxations, which gradually close the hysteresis curve during discharge start below ≈ 110 mAh g^{-1}. The further the cell is discharged below this point, the more domains can overcome their individual barriers and remain in the relaxed state with its corresponding entropy and OCV, even if the cell is recharged back to the reference capacity (C_0). This is in agreement with literature reports on the OCV hysteresis[44,58] and the hysteresis of lattice parameters.[5,6] For example, Croy et al.,[44] found that the voltage hysteresis upon discharge in the range between 4.6 V (translates to $\xi \approx 0.96$ in our case) and 3.8 V ($\xi \approx 0.66$) is almost non-existent, but gradually grows when the window is further opened up to 3.3 V ($\xi \approx 0.24$). Also, Teufl et al.,[1] report on an increasing path dependence of the resistance with increasing upper cutoff voltage during charge. Figure S8 in the Supporting Information shows a window-opening experiment during charge, which was conducted in a similar manner as the one shown in Fig. 5 (procedure explained in the SI). Starting at an SOC of $C_0 = 100$ mAh g^{-1}, charge-discharge loops to increasing upper cut-offs were conducted. The entropy and OCV measured after reaching C_0 again indicate that the relaxation processes during charge occur when the cell is charged above ≈ 150 mAh g^{-1}.

We can conclude that on the metastable pathways of the hysteresis loop, the LMR-NCM material can behave quasi-reversible in some sections, and endure irreversible relaxations in other sections. The nature of the energy barriers in LMR-NCM cannot be clarified by the applied entropy measurement. Instead, we observe the effect that the hysteresis has on the entropy profile, namely a path-dependence of the entropy curve vs SOC between charge and discharge. We want to stress once more that the peak in the 0.33 LMR-NCM/Li entropy curve, which might indicate a second order phase transition, must be regarded as another phenomenon.

Entropy and reversible heat in LMR-NCM.—The integral of the charge or discharge voltage curve over the SOC corresponds to the electrical energy applied during charge and gained during discharge. The difference of both corresponds to the energy loss in form of heat over a complete cycle. The irreversible heat (Q_{irrev}) due to charge transfer and mass transport overpotential losses leads to a difference between the potential E at an applied current I and the equilibrium potential E_0 at OCV conditions. In Fig. 3, Q_{irrev} corresponds to the area between the black line (voltage while applying a current) and the blue line (OCV curve). The irreversible heat scales with the applied current and is always exothermic. The energy loss corresponding to the OCV hysteresis (blue area in Fig. 3) is independent of the applied current (see Fig. S6 in the SI). The description of this heat term is not trivial and will be the focus of a different study.[59] Additionally, heat can be released and absorbed reversibly because of entropic changes in the battery. In contrast to the other sources of heat, this cannot be derived from the voltage curve. The reversible heat generation, Q_{rev}, is a function of the partial molar entropy and the temperature. For a reversible process, Q_{rev} is obtained by:

$$Q_{rev} = \int T \cdot \left(\frac{dS}{d\xi}(\xi) \right) \cdot d\xi \qquad [16]$$

In the case of LMR-NCM, however, ξ does not describe the charge/discharge processes unambiguously. Particularly, at the same ξ, the CAM can have two different structures evidenced by the observed differences in lattice parameters[5,6] and atomic distances.[7] The OCV hysteresis furthermore underlines that the re-entrant Li environment during discharge is energetically different from that during charge.[4,46] In fact, it is known that hysteretic processes follow metastable paths away from the thermodynamic equilibrium.[43,60] The measurement of the cell-TD-OCV, however, can only trace the chemical potential along the accessible metastable pathway. In case of the LMR-NCM, frustrated structural relaxations might induce this metastability. In the course of the hysteresis loop, some of the energetic barriers to equilibrium may eventually sink so that irreversible relaxations can partially or locally restore equilibrium

and release structural or chemical energy. In a closed cycle, all the additionally produced entropy eventually has to be transferred to the surrounding in order to ensure entropy conversion. This entropy transfer does not necessarily occur immediately, as long as it does not arrive at motional degrees of freedom leading to a temperature increase. It can happen later during further progress of charging or discharging. Under isothermal conditions, the entropy will be transferred in a reversible act and so structural or chemical energy is finally carried to the surroundings in form of heat. The total entropy change of the system, dS_{sys}, for materials with a pronounced hysteresis can thus be written as:

$$dS_{sys} = dS_{equi} + dS_{int,prod} \quad [17]$$

dS_{equi} is the entropy change of the system, if it were in equilibrium and could reversibly exchange heat with the surroundings. The corresponding reversible heat is calculated based on integrating dS_{equi} according to Eq. 16. Since entropy is a state function, it is conserved for reversible processes, meaning that $\oint dS_{equi} = 0$. For LMR-NCM, another term is required, which describes the internal entropy production, $dS_{int,prod}$.[43,57,60] This is the additional entropy change of the system, which occurs due to redistribution of energy during structural relaxation. Such relaxations bring any hysteretic deviations of the state functions closer to equilibrium and internally "produce" entropy. Experimentally, only the total entropy change of the system, dS_{sys}, is accessible and we do not know, how large dS_{equi} actually is. It should, however, not suffer from hysteresis and should thus be the same for charging and discharging (with opposite sign) and be zero when a complete cycle is considered. Due to the additional term of $dS_{int,prod}$ in case of LMR-NCM, a cyclic integral over the measured partial molar entropy will, however, not be zero but be a measure of the internal entropy production within a complete cycle. Interpretation of this integral requires a bit of care. For clarity, we split the integration of the measured partial molar entropy of LMR-NCM in two parts. The integration of $\frac{dS}{d\xi}(\xi)$ over ξ gives $\approx+10.0$ J (mol K^{-1}) for the charge and ≈-11.2 J (mol K^{-1}) for the discharge process (for $0.11 \leqslant \xi \leqslant 0.91$; $d\xi > 0$ for charge and $d\xi < 0$ for discharge). The observed difference is a measure of the internal entropy production. It is surprising that the cyclic integral over the whole charge/discharge process gives has negative sign although entropy production is expected to be positive. The observed difference can hence not solely be explained by irreversible processes with entropy change being strictly positive. The formation of products with lower entropy during charge or higher entropy during discharge could explain this unusual observation. It is well known that LMR-NCM suffers from ongoing voltage decay[61,62] which is proposed to be caused by progressive irreversible TM migration[61,63] possibly coupled to oxygen redox[45] and even oxygen vacancies.[64] Moreover, the formation of an oxygen depleted surface layer is reported to cause capacity fading over cycling.[31] For such structural transformations, the sign of the entropy change is not known and they might hence explain the observed negative value. A contribution of entropy production (with positive sign) can nevertheless not be excluded. The observed difference between the charge and discharge entropy curve needs to be interpreted with care since we have to consider, how reliable the determination of $\frac{dS}{d\xi}(\xi)$ is. We are confident that the observed shift between the charge and the

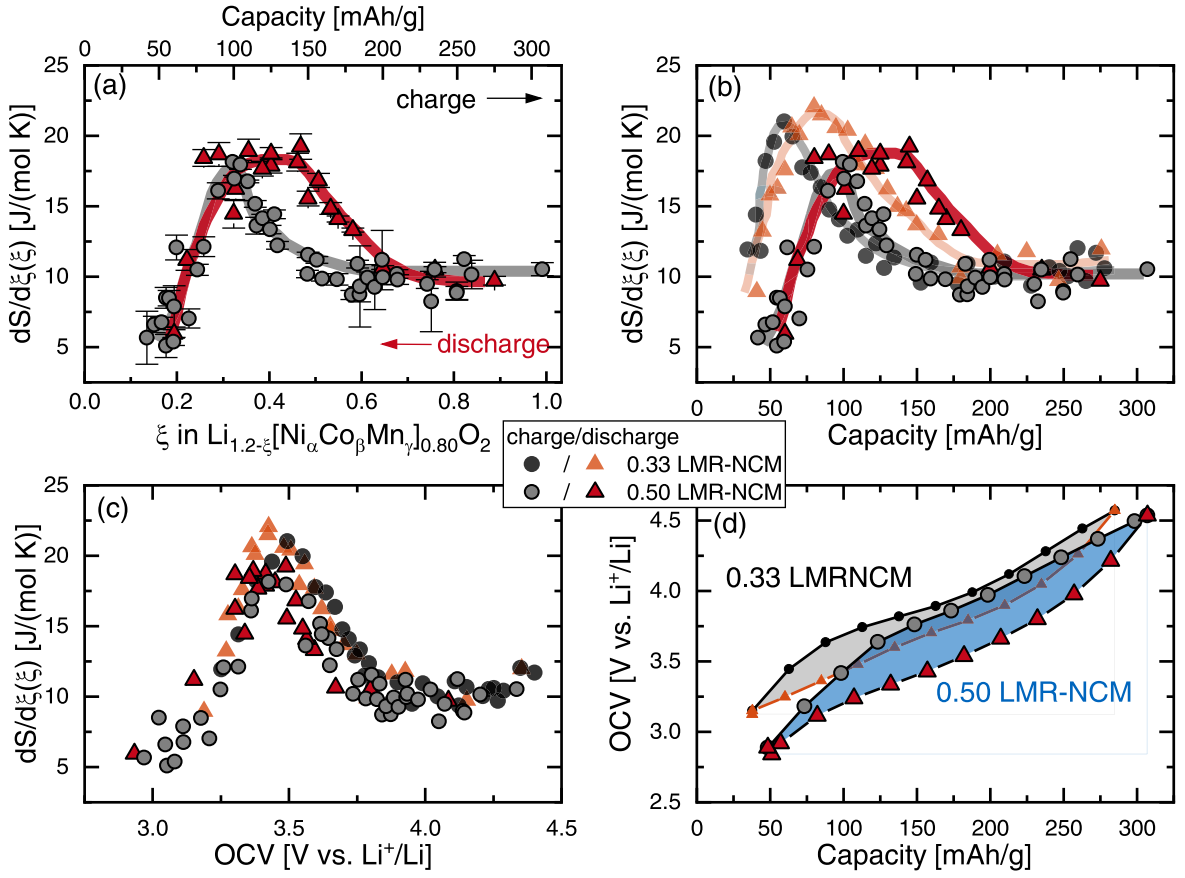

Figure 6. (a) Partial molar entropy data and trendlines (as guide for the eye) vs capacity (upper x-axis) or ξ (lower x-axis) of 0.50 LMR-NCM/Li cells during charge (gray circles) and discharge (red triangles) after one activation and two stabilization cycles. (b) Comparison of $\frac{\partial S}{\partial \xi}(\xi)$ vs capacity for 0.50 LMR-NCM/Li (same color code as in panel a) and for 0.33 LMR-NCM/Li cells (black circles for charge, orange triangles for discharge; same data as in Fig. 4b), with error bars removed for clarity. (c) Comparison of the same $\frac{\partial S}{\partial \xi}(\xi)$ data but plotted as a function of OCV. (d) OCV curves comparing the OCV hysteresis of 0.50 LMR-NCM/Li (blue) and 0.33 LMR-NCM/Li cells (gray; same data as in Fig. 3) at C/10 (25 °C) after activation and two stabilization cycles.

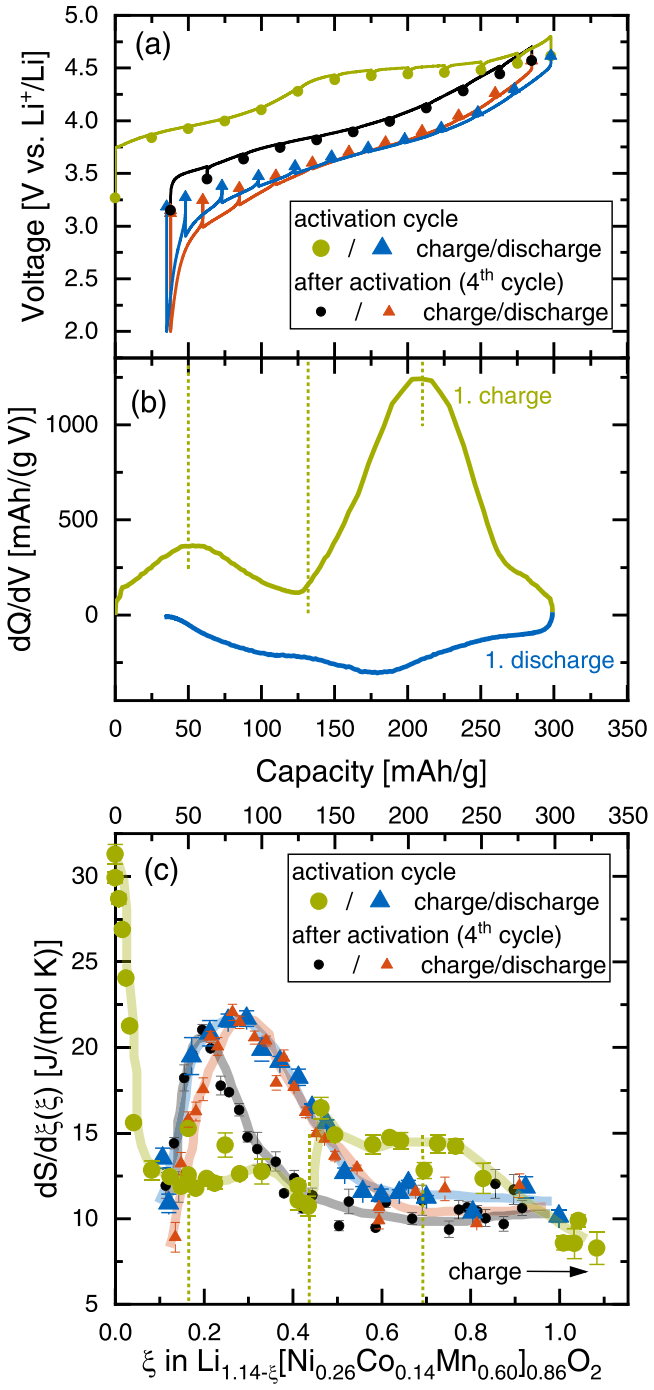

Figure 7. Comparison of voltage and partial molar entropy vs capacity curves during activation and after activation/stabilization (4th cycle) of 0.33 LMR-NCM/Li cells with trendlines as guides for the eye (all at 25 °C): (a) voltage curves with OCV points of the activation cycle at C/15 (charge in green, discharge in blue) and of the 4th cycle (C/10, charge in black, discharge in orange); (b) dQ/dV plot of the activation of a LMR-NCM/Li cell at C/15; (c) partial molar entropy values during charge (circles) and discharge (triangles) in the activation cycle (green/blue) and the 4th cycle (black/orange) as a function of capacity (upper x-axis) and ξ (lower x-axis). The dashed vertical lines highlight common features in the different plots.

discharge entropy curves is true. The shift, however, is not the reason for the observed difference. Instead, the peak of the $\frac{dS}{d\xi}(\xi)$ curve during discharge is slightly broader than during charge. The difference between both only amounts to ≈ 10% of the absolute values. Considering the pronounced scatter of the data points in Fig. 4, the interpretation of this value requires a bit of care. In summary, we conclude that the calculation of the classical reversible heat according to Eq. 16 as a function of SOC is not applicable for materials with a pronounced hysteresis such as LMR-NCM since the measured entropy includes contributions from internal entropy production.

Effect of overlithiation on the entropy profile of LMR-NCM.— *Entropy profile of 0.50 LMR-NCM.*—To further analyze the entropy of this type of CAMs, the measurements were repeated on an LMR-NCM with a higher degree of overlithiation. The standard material of this study was denoted as 0.33 LMR-NCM ($Li_{1.14}[Ni_{0.26}Co_{0.14}Mn_{0.6}]_{0.86}O_2$), while 0.50 LMR-NCM refers to the material with the higher Li content, with the overall stoichiometry of $Li_{1.20}[TM]_{0.80}O_2$. The nomenclature and stoichiometry are explained in the Experimental section. It was shown in the literature that the degree of overlithiation in LMR-NCM affects the electrochemical performance of this CAM class in terms of surface degradation and resistance build-up, but also with regards to the lattice parameters.[6,31,58] As can be seen in Fig. 6d, the size of the OCV hysteresis loop increases with the degree of overlithiation. This is expressed in terms of a ≈ 1.5-fold increase in the OCV hysteresis related energy loss over the same ΔSOC that is represented by the gray and blue shaded areas in Fig. 6d (45.5 mWh g^{-1} vs 69.2 mWh g^{-1}), caused by a ≈ 1.5 -fold increase in the ΔSOC averaged mean voltage difference between the charge and discharge OCV curves (184 mV vs 268 mV; obtained by dividing the OCV hysteresis energy by the ΔSOC window of 247 mAh g^{-1} for 0.33 LMR-NCM and 259 mAh g^{-1} for 0.50 LMR-NCM).

Figure 6a shows the $\frac{\partial S}{\partial \xi}(\xi)$ vs SOC (and ξ) profile of 0.50 LMR-NCM/Li cells, obtained from cell-TD-OCV measurements after one activation and two stabilization cycles. Similar to the curves of the 0.33 LMR-NCM/Li (see Fig. 4b), there is a path dependence of the partial molar entropy between charge and discharge, with a peak around ξ ≈ 0.3 during charge and a broader peak at ξ ≈ 0.4 during discharge. In Fig. 6b, the $\frac{\partial S}{\partial \xi}(\xi)$ profiles of LMR-NCM/Li cells with either 0.33 LMR-NCM or 0.33 LMR-NCM are contrasted. To enable a comparison of the two materials on the SOC scale, the data are shown as a function of capacity rather than extent of reaction because ξ was defined relative to the total amount of Li, which differs for both materials. The most remarkable difference between the partial molar entropy profiles of the LMR-NCM materials in Fig. 6b is the shift of the partial molar entropy peaks in both charge and discharge to higher SOC values for the 0.50 LMR-NCM (gray and red symbols) compared to the 0.33 LMR-NCM (black and orange symbols); hereby, only the positions of the peak maxima are shifted, while the partial molar entropy values to the right of the peaks (i.e., at higher SOCs) become practically identical for both materials in both the charge and the discharge direction. Moreover, the peak maxima of the 0.50 LMR-NCM are lower by an absolute value of ≈ 4 J/(mol K). Both materials have in common that their discharge peaks are rather broad in comparison to the respective charge peaks and that the partial molar entropy values reach the same plateau values at high degrees of delithiation. The path dependence expressed in terms of peak shifting between charge and discharge is very similar for both materials with ΔSOC ≈ 23 mAh/g (≈ 6.1% of the total Li amount in $Li_{1.20}[TM]_{0.80}O_2$) for the 0.50 LMR-NCM and ΔSOC ≈ 22 mAh g^{-1} (≈ 6.4% referenced to $Li_{1.14}[TM]_{0.86}O_2$) for the 0.33 LMR-NCM. From the increased OCV hysteresis loop of the 0.50 LMR-NCM, shown in Fig. 6d, one might have expected that the partial molar entropy profile of this material would show a considerably larger peak shift, which is not the case. Interestingly, when plotted as a function of OCV, as is shown in Fig. 6c, the partial molar entropy profiles in charge and discharge for both materials superimpose aside from the smaller peak heights for the 0.50 LMR-NCM. This means that not only the material specific path dependence has vanished vs OCV but also the difference

between the materials. We conclude that although the OCV hysteresis curves of these materials are different (see Fig. 6d), the entropy profiles coincide when considered as a function of OCV.

Indications for vibrational entropy.—As discussed above, the changes in vibrational entropy are expected to be a function of the OCV and not of the SOC, whereas the configurational entropy should be a function of ξ and hence of the SOC. The fact that the differences in the partial molar entropy profiles between the two LMR-NCM materials plotted vs SOC vanish when they are plotted as a function of OCV suggests that independent of the apparent SOC, the OCV is the actual descriptor of the electrochemical state of the material. In other words, when two LMR-NCM materials are considered to be at the same OCV, they might have a different amount of Li, which can be distributed over the available Li sites, but nevertheless they have the same value for $\frac{dS}{d\xi}(\xi)$. This is another strong indicator that what we observe in the $\frac{dS}{d\xi}(\xi)$ curve cannot be dominated by the configurational entropy but rather by the vibrational entropy of the host lattice. From a theoretical point of view, a thorough simulation of the LMR-NCM structure at different SOCs and the respective derivation of vibrational density of states could shed more light on this issue.

Partial molar entropy during the first-charge activation of LMR-NCM.— *Partial molar entropy of LMR-NCM before and after activation.*—For LMR-NCM cathode active materials, it is well known that during the first charge a so-called activation process occurs, during which oxygen is released from the material[31,65] and irreversible structural changes[45,66] occur, including transition metal migration, oxygen redox, and the loss of a honeycomb ordering. These irreversible processes lead to a unique first charge voltage curve and also cause the cell resistance[1] and the lattice parameters[6] to differ from that of the following cycles. Hence, we also expect a unique partial molar entropy profile during the activation of LMR-NCM. In Fig. 7a, the voltage profile of the first activation cycle is compared to that of the 4th cycle, where all other entropy measurements were typically conducted. In addition to an initial voltage plateau around ≈4 V, the first charge curve exhibits a characteristic second plateau at ≈4.5 V (green line). Both features become more obvious from the corresponding peaks in the dQ/dV plot in Fig. 7b (green line). In contrast, the first discharge (blue line in Fig. 7a) resembles all following discharge curves after activation, as represented by the 4th cycle (orange line).

In Fig. 7c, the partial molar entropy changes during activation are compared to those after activation (measured in the 4th cycle, as shown in Fig. 4). The entropy curve in the first activation charge (green circles) is completely different from that obtained during the charge of a cell after activation/stabilization (black circles). At the beginning of the first charge ($\xi = 0$), the most positive partial molar entropy is observed, decreasing in a pole-like feature which levels off to a value of ≈ 12 J (mol K^{-1}) at ≈ 50 mAh g^{-1}. This transition point coincides with the first maximum in the dQ/dV plot (marked by the first set of vertical green dashed lines in Fig. 7), i.e., in the mid-point of the first voltage plateau. At a capacity of ≈ 130 mAh g^{-1}, a double pole feature is observed, first going down and then switching to a second pole coming from more positive values of $\frac{dS}{d\xi}(\xi)$. This feature coincides with the transition to the second voltage plateau that is marked by the minimum in the dQ/dV plot in Fig. 7b (second set of green dashed lines in Fig. 7). Subsequently, the $\frac{dS}{d\xi}(\xi)$ profile remains rather flat in the SOC range around ≈ 200 mAh g^{-1}, where another dQ/dV maximum occurs marking the middle of the second voltage plateau (third set of green dashed lines in Fig. 7). Starting at ≈ 250 mAh g^{-1}, $\frac{dS}{d\xi}(\xi)$ gradually decreases to ≈ 8 J (mol K^{-1}) at the end of charge. During the first activation charge, there is no indication of the prominent broad peak at $\xi \approx 0.2$ seen during charging of LMR-NCM after activation (black circles/lines in Fig. 7c).

In contrast to these striking differences observed during charge, there is no considerable difference between the entropy curve of the first and the 4th discharge (blue and orange symbols in Fig. 7b), in accordance to the associated voltage curves (see Fig. 7a). Window opening experiments in the activation charge show the same trend as was found for the LMR-NCM/Li cells after the initial activation/stabilization cycles. In Fig. S9 in the SI it can be seen that, when the charge window is gradually opened, the entropy values measured at a reference capacity point (C_0 = 75 mAh g^{-1}) subsequently change and shift from the first charge profile to that of the first discharge profile.

Although the entropy data of Shi et al.[48] obtained after the initial activation/stabilization cycles differ from ours, as already noted, they likewise observe significant differences between the entropy profiles during the first charge and the following charge cycles. In their data, the peak at low SOC during charge is also missing during activation, whereas during discharge they see a comparable curve shape as in their following cycles including a peak-like feature at low SOCs.

Configurational entropy during the first charge of LMR-NCM.—In the following we will put our results into context with literature reports that have investigated the activation process in this type of materials with other methods. The positive pole in the $\frac{dS}{d\xi}(\xi)$ curve near $\xi = 0$ (green circles in Fig. 7c) is a typical and strong indication of emerging configurational freedom of Li in the host lattice after the first empty Li-sites become available. In such a case, one expects a typical S-shaped $\frac{\partial S}{\partial \xi}(\xi)$ dependence.[13–15] The corresponding negative pole might appear at $\xi \approx 0.4$ back to back with a second positive pole. A closing negative pole expected from the last exchangeable Li emanating from the host sites appears only in outlines beyond $\xi > 0.9$, if at all. The back to back pole pairs reflect switching between pools of energetically equivalent sites similar to what is reported for the two sub-lattice model[13–15] mentioned above. Such a discontinuity in the entropy curve at $\xi \approx 0.4$ might be caused by a sufficiently high difference in the interaction energy of the Li with the two sites,[15] which would be consistent with the observations that the mid-points of the low and high voltage plateau, as indicated by the maxima in the dQ/dV plot, differ by ≈ 0.5 V (first and last set of the green dashed lines in Figs. 7b and 7c). The discontinuity could, in principle, also be caused by pronounced repulsive nearest neighbor interactions.[13] In contrast to the succeeding cycles, where no sign of configurational entropy was found, entropy data of the first charge give strong evidence for free Li exchange between sites being cleared in two consecutive voltage steps. A significant amount of Li sites are therefore energetically equivalent (within thermal energy) between $\xi \approx 0$ and $\xi \approx 0.4$, at which point a second pool of energetically equivalent sites starts to allow for Li exchange. Since there is no clear signature of a final negative pole at high SOC, it cannot be specified up to which values of ξ this exchange persists. Two successive pools of energetically equivalent sites would also be in agreement with the two characteristic plateaus in the first charge voltage profile. Both findings suggest that the delithiation actuates (at least) two different charge compensation mechanisms.[50,66,67]

During the initial plateau associated with the first peak in the dQ/dV plot, cationic oxidation of Ni and Co occurs. This process is the same as for classical layered transition metal oxide cathodes. When LMR-NCM cathodes are only cycled within this limited SOC range ($\xi < 0.4$), they behave like stoichiometrically lithiated NCMs, meaning that the hysteresis of the voltage,[44] of the lattice parameters,[6] and the resistance[1] is minor. Likewise, the entropy profile of LMR-NCM in this first region, also resembles those observed for regular NCMs.[9,48] Window-opening experiments during the first charge (Figure S9 in the SI) show that the entropy

profile is maintained and is not path dependent as long as the material is not cycled beyond $\xi \approx 0.4$.

In contrast to the initial low-voltage plateau of the activation process, the subsequent high-voltage plateau is reported to include irreversible changes within the LMR-NCM such as O-redox occurring together with TM migration and the removal of Li from the TM layer.[50,66–68] The oxidation of O^{2-} is reported to be mostly reversible for the bulk oxygen,[45,66,67] at the surface, however, O_2 is irreversibly lost from the structure.[65] On charging across the high-voltage plateau, the in-plane honeycomb superstructure ordering of the TMs is irreversibly lost.[45,66] A coupling between TM migration and bulk anionic redox is discussed in the literature.[45,66] The fact that the activation charge of LMR-NCM proceeds via two different charge compensation steps, of which the first is reversible while during the second step the LMR-NCM structure is permanently modified, is a strong indication that the interpretation of the corresponding entropy curve with two pools of energetically equivalent sites is valid. As mentioned above, we do not propose two crystallographically different sub-lattices, but rather two energetically different Li deintercalation processes. The contributions of the configurational entropy during the first charge seem to be responsible for the observed entropy curve features (on the order of ± 2 J (mol K^{-1})), but the entropy offset of -12 J (mol K^{-1}) is not related to configurational contributions.

In contrast to the unique entropy curve upon the first activation charge, there is no considerable difference between the entropy curve of the first and the 4th discharge, which also reflects the behavior of the voltage curves. This means that the (de-)intercalation processes within the LMR-NCM material during the first charge differ significantly from those of the first discharge and of all consecutive cycles. The fact that the features from the configurational entropy are no longer observable in the first discharge indicates that the model of two pools of energetically equivalent Li sites is no longer appropriate to describe the Li (de-)intercalation process. Apparently, the distributional variability of Li among empty lattice sites is effectively hindered. From the literature it is known that the LMR-NCM structure is permanently modified during the activation process. Although the bulk anionic redox is continuously reversed upon discharge, the reordering of the TM layer is not possible and the honey-comb superstructure is lost, which changes the coordination environment around the oxygen.[45,66] Furthermore, NMR studies show that, in the fully discharged state, the local environment of Li is different from that of the pristine state, revealing a much higher degree of disorder in the TMs surrounding the Li.[66] These irreversible structural modifications lead to a permanently lowered voltage profile upon subsequent cycling, with an increased slope as compared to the first charge voltage curve[45,67] and to a smaller peak amplitude in the respective dQ/dV plots (compare Figs. 7b and 4b). As a consequence, the Li sites are energetically wider dispersed, which reduces the configurational freedom of Li within the lattice and hence blurs any features from configurational entropy leaving back the more dominant contribution from the vibrational entropy. Whether the processes which are responsible for the observed disappearance of the configurational entropy are also responsible for the hysteretic behavior of the LMR-NCM remains an open question. Qiu et al.[69] recently reported that after activation, the pristine state of LMR-NCM cannot be recovered by normal cycling but they demonstrated that the structure of cycled LMR-NCM can be driven close to the original pristine state by heat treatment. For this purpose, they harvested CAM after 50 regular cycles, heat treated the material at up to 300 °C and built new cells with the heat treated CAM.[69] They observe a reappearance of the plateau region at ≈ 4.5 V in the voltage vs capacity plot, which they ascribe to the lithium ion reinsertion into the TM layer and the reduction of stacking faults and microstrain.[69] It would be very interesting to investigate if a heat treatment of the LMR-NCM after activation also leads to a recovery of the partial molar entropy curve from the first charge including the fingerprints from configurational entropy.

Conclusions

The partial molar entropy changes $\frac{dS}{d\xi}(\xi)$ of LMR-NCM/Li cells during lithium (de-)intercalation were investigated. To obtain $\frac{dS}{d\xi}(\xi)$, the OCV variation of the cell needs to be measured as a function of temperature. We evaluated the experimental methods applied so far and found that the widely implemented temperature step method is prone to measurement artefacts. Instead, we implemented a temperature ramp method, where the response of the OCV during a triangular wave variation of the cell temperature is measured. Effects from self-discharge, ongoing voltage relaxation and temperature history can thereby be minimized.

To distinguish between the contribution of the LMR-NCM and the Li electrode, the latter was first analyzed by means of spatially non-isothermal experiments. We have found that the contribution of Li (≈ 1.1 mV K^{-1}) is in the same order of magnitude as the contribution of the cathode and only the difference between the two leads to the small values (≈ -0.1 mV K^{-1}) observed for the LMR-NCM/Li cell under spatially isothermal conditions. Since we measure the OCV of LMR-NCM vs the Li reference electrode in all following experiments, we can assume that the contribution of Li is constant as a function of SOC and that all features observed in the $\frac{dS}{d\xi}(\xi)$ curve of LMR-NCM/Li cells originate from processes in the cathode.

The cathode active material in the focus of this study is LMR-NCM, which exhibits a unique hysteresis in the OCV. The resulting partial molar entropy curves of LMR-NCM/Li cells show no typical fingerprint features of the configurational entropy indicating that there is hardly any configurational freedom of Li within the LMR-NCM. In fact, from the steepness of the OCV curve, we do not expect to find enough exchangeable Li within the Li layers to contribute to configurational entropy. Instead, the entropy profile is dominated by the changes in the lattice entropy (vibrational entropy). We found a broad peak in the $\frac{dS}{d\xi}(\xi)$ curve, similar to a feature of a second order phase transition. Since diffraction studies have not reported any evidence for a second phase, we propose that there is no crystallographic phase transition but rather a change in the local ordering or the energetics of the lattice (e.g. lattice strain). We observed a hysteresis of the characteristic peak in the $\frac{dS}{d\xi}(\xi)$ curve as a function of SOC, which vanishes if mapped as a function of OCV revealing that the entropy changes in LMR-NCM are governed by the OCV and thus by the Gibbs free energy and not by the amount of Li in the structure (ξ). This trend was also observed for an LMR-NCM material with a higher degree of overlithiation. Clearly, ξ is no unique descriptor of the (de-)lithiation processes within LMR-NCM because at the same ξ, LMR-NCM has a different structure evidenced by OCV and $\frac{dS}{d\xi}(\xi)$ values. This means that the charge and discharge processes do not follow reversible pathways when a full cycle is considered, which was further shown by window-opening experiments. We conclude that the (de-)lithiation of LMR-NCM follows metastable paths away from thermodynamic equilibrium, as is common for hysteretic processes. In order to determine the reversible heat of a battery, the partial molar entropy curve is typically integrated. For LMR-NCM, this, however, also includes an additional term caused by internal entropy production.

In addition to the analysis of a reversible cycle (after activation and stabilization), the entropy profile of LMR-NCM/Li was also investigated during the first activation cycle. The resulting $\frac{dS}{d\xi}(\xi)$ curve obtained during the first charge differs significantly from that

of the first discharge and of subsequent cycles. We explain the observed curve features with changes in the configurational entropy according to a two sub-lattice model. Apparently, the material undergoes a permanent transformation during this activation, which diminishes the distributional variability of Li ions in the structure and hence blurs the contribution from the configurational entropy for all subsequent charge/discharge processes.

Our findings on hysteresis, the resonance feature detected in entropy and the observed dependence on OCV should stimulate and focus detailed investigations with other experimental methods on these features, which could lay the basis for extensive quantum chemical calculations.

Acknowledgments

This work was supported by BASF SE within its Battery Research Network. The authors want to thank Alexander Ogrodnik for his contributions to this manuscript.

ORCID

Franziska Friedrich https://orcid.org/0000-0001-9400-1212
Hubert A. Gasteiger https://orcid.org/0000-0001-8199-8703

References

1. T. Teufl, D. Pritzl, S. Solchenbach, H. A. Gasteiger, and M. A. Mendez, *J. Electrochem. Soc.*, **166**, A1275 (2019).
2. J. Chen, A. Gutierrez, M. T. Saray, R. S. Yassar, M. Balasubramanian, Y. Wang, and J. R. Croy, *J. Electrochem. Soc.*, **168**, 080506 (2021).
3. S. R. Gowda, D. W. Dees, A. N. Jansen, and K. G. Gallagher, *J. Electrochem. Soc.*, **162**, A1374 (2015).
4. F. Dogan, B. R. Long, J. R. Croy, K. G. Gallagher, H. Iddir, J. T. Russell, M. Balasubramanian, and B. Key, *J. Am. Chem. Soc.*, **137**, 2328 (2015).
5. H. Konishi, T. Hirano, D. Takamatsu, A. Gunji, X. Feng, S. Furutsuki, T. Okumura, S. Terada, and K. Tamura, *J. Solid State Chem.*, **262**, 294 (2018).
6. B. Strehle, T. Zünd, S. Sicolo, A. Kießling, V. Baran, and H. A. Gasteiger, *J. Electrochem. Soc.* (2021), In Press.
7. H. Koga, L. Croguennec, M. Ménétrier, P. Mannessiez, F. Weill, C. Delmas, and S. Belin, *J. Phys. Chem.C.*, **118**, 5700 (2014).
8. K. Maher and R. Yazami, *J. Power Sources*, **247**, 527 (2014).
9. E. Schuster, C. Ziebert, A. Melcher, M. Rohde, and H. J. Seifert, *J. Power Sources*, **286**, 580 (2015).
10. V. V. Viswanathan, D. Choi, D. Wang, W. Xu, S. Towne, R. E. Williford, J. G. Zhang, J. Liu, and Z. Yang, *J. Power Sources*, **195**, 3720 (2010).
11. A. Eddahech, O. Briat, and J. Vinassa, *Energy*, **61**, 432 (2013).
12. K. Takano, Y. Saito, K. Kanari, K. Nozaki, K. Kato, A. Negishi, and T. Kato, *J. Appl. Electrochem*, **32**, 251 (2002).
13. S. Schlueter, R. Genieser, D. Richards, H. E. Hoster, and M. P. Mercer, *Phys. Chem. Chem. Phys.*, **20**, 21417 (2018).
14. M. P. Mercer, S. Finnigan, D. Kramer, D. Richards, and H. E. Hoster, *Electrochim. Acta*, **241**, 141 (2017).
15. E. P. M. Leiva, E. Perassi, and D. Barraco, *J. Electrochem. Soc.*, **164**, A6154 (2017).
16. T. Liebmann, C. Heubner, M. Schneider, and A. Michaelis, *J. Solid State Electrochem.*, **23**, 245 (2019).
17. M. Song, Y. Hu, S.-Y. Choe, and T. R. Garrick, *J. Electrochem. Soc.*, **167**, 120503 (2020).
18. K. Kai, Y. Kobayashi, H. Miyashiro, G. Oyama, S.-I. Nishimura, M. Okubo, and A. Yamada, *ChemPhysChem*, **15**, 2156 (2014).
19. S. L. Glazier, S. A. Odom, A. P. Kaur, and J. R. Dahn, *J. Electrochem. Soc.*, **165**, A3449 (2018).
20. Y. Reynier, J. Graetz, T. Swan-Wood, P. Rez, R. Yazami, and B. Fultz, *Phys. Rev. B*, **70**, 174304 (2004).
21. Y. Reynier, R. Yazami, and B. Fultz, *J. Power Sources*, **119–121**, 850 (2003).
22. X.-F. Zhang, Y. Zhao, Y. Patel, T. Zhang, W.-M. Liu, M. Chen, G. J. Offer, and Y. Yan, *Phys. Chem. Chem. Phys.*, **19**, 9833 (2017).
23. P. Gründler, A. Kirbs, and L. Dunsch, *ChemPhysChem*, **10**, 1722 (2009).
24. J. R. Dahn and R. R. Haering, *Can. J. Phys.*, **61**, 1093 (1983).
25. A. Swiderska-Mocek, E. Rudnicka, and A. Lewandowski, *Phys. Chem. Chem. Phys.*, **21**, 2115 (2019).
26. A. J. DeBethune, T. S. Licht, and N. Swendeman, *J. Electrochem. Soc.*, **106**, 616 (1959).
27. J. L. Valdes and B. Miller, *J. Phys. Chem.*, **92**, 4483 (1988).
28. E. Maciá-Barber, *Thermoelectric Materials:Advances and Applications* (CRC Press, Boca Raton) (2015).
29. J. K. Platten, *J. Appl. Mech.*, **73**, 5 (2006).
30. M. A. Rahman and M. Z. Saghir, *Exp. Therm. Fluid Sci.*, **49**, 31 (2013).
31. T. Teufl, B. Strehle, P. Müller, H. A. Gasteiger, and M. A. Mendez, *J. Electrochem. Soc.*, **165**, A2718 (2018).
32. D. Schreiner, T. Zünd, F. J. Günter, L. Kraft, B. Stumper, F. Linsenmann, M. Schüßler, R. Wilhelm, A. Jossen, G. Reinhart, and H. A. Gasteiger, *J. Electrochem. Soc.*, **168**, 030507 (2021).
33. S. Solchenbach, D. Pritzl, E. J. Y. Kong, J. Landesfeind, and H. A. Gasteiger, *J. Electrochem. Soc.*, **163**, A2265 (2016).
34. K. Jalkanen, T. Aho, and K. Vuorilehto, *J. Power Sources*, **243**, 354 (2013).
35. Y. Abdul-Quadir, T. Laurila, J. Karppinen, K. Jalkanen, K. Vuorilehto, L. Skogström, and M. Paulasto-Kröckel, *Int. J. Energy Res*, **38**, 1424 (2014).
36. Y. F. Reynier, R. Yazami, and B. Fultz, *J. Electrochem. Soc.*, **151**, A422 (2004).
37. I. Zilberman, A. Rheinfeld, and A. Jossen, *J. Power Sources*, **395**, 179 (2018).
38. L. M. Housel, W. Li, C. D. Quilty, M. N. Vila, L. Wang, C. R. Tang, D. C. Bock, Q. Wu, X. Tong, A. R. Head, K. J. Takeuchi, A. C. Marschilok, and E. S. Takeuchi, *ACS Appl. Mater. Interfaces*, **11**, 37567 (2019).
39. P. J. Osswald, M. del Rosario, J. Garche, A. Jossen, and H. E. Hoster, *Electrochim. Acta*, **177**, 270 (2015).
40. K. E. Thomas, C. Bogatu, and J. Newman, *J. Electrochem. Soc.*, **148**, A570 (2001).
41. Q. Huang, M. Yan, and Z. Jiang, *J. Power Sources*, **156**, 541 (2006).
42. P. J. Linstrom and W. G. Mallard, *NIST Chemistry WebBook* (National Institute of Standards and Technology, Gaithersburg MD) (2020).
43. E. Neumann (ed.), *Angew. Chem. Int. Ed. Engl.*, **12**, 356 (1973).
44. J. R. Croy, K. G. Gallagher, M. Balasubramanian, Z. Chen, Y. Ren, D. Kim, S.-H. Kang, D. W. Dees, and M. M. Thackeray, *J. Phys. Chem. C*, **117**, 6525 (2013).
45. W. E. Gent, K. Lim, Y. Liang, Q. Li, T. Barnes, S. Ahn, K. H. Stone, M. McIntire, J. Hong, J. H. Song, Y. Li, A. Mehta, S. Ermon, T. Tyliszczak, D. Kilcoyne, D. Vine, J. Park, S. Doo, M. F. Toney, W. Yang, D. Prendergast, and W. C. Chueh, *Nat. Commun.*, **8**, 2091 (2017).
46. K. Ariyoshi, T. Inoue, and Y. Yamada, *J. Electrochem. Soc.*, **165**, A2675 (2018).
47. T. Ohzuku, M. Nagayama, K. Tsuji, and K. Ariyoshi, *J. Mater. Chem.*, **21**, 10179 (2011).
48. W. Shi, J. Zheng, J. Xiao, X. Chen, B. J. Polzin, and J.-G. Zhang, *J. Electrochem. Soc.*, **163**, A571 (2016).
49. B. Manikandan, C. Yap, and P. Balaya, *J. Electrochem. Soc.*, **164**, A2794 (2017).
50. G. Assat and J. Tarascon, , *Nat. Energy*, **3**, 373 (2018).
51. Y. Saito, K. Takano, K. Kanari, A. Negishi, K. Nozaki, and K. Kato, *J. Power Sources*, **97–98**, 688 (2001).
52. C. Heubner, S. Heiden, M. Schneider, and A. Michaelis, *Electrochim. Acta*, **233**, 78 (2017).
53. X. Gong, J. Huang, Y. Chen, M. Wu, G. Liu, X. Lei, J. Liang, H. Cao, F. Tang, B. Xu, and C. Ouyang, *Int. J. Electrochem. Sci.*, **8**, 10549 (2013).
54. N. P. Butch, M. E. Manley, J. R. Jeffries, M. Janoschek, K. Huang, M. B. Maple, A. H. Said, B. M. Leu, and J. W. Lynn, *Phys. Rev. B*, **91**, 035128 (2015).
55. J. R. Morris and R. J. Gooding, *Phys. Rev. Lett.*, **65**, 1769 (1990).
56. W. R. McKinnon, J. R. Dahn, J. J. Murray, R. R. Haering, R. S. McMillan, and A. H. Rivers-Bowerman, *J. Phys. C Solid State Phys.*, **19**, 5135 (1986).
57. G. Assat, S. L. Glazier, C. Delacourt, and J.-M. Tarascon, *Nat. Energy*, **4**, 647 (2019).
58. J. R. Croy, K. G. Gallagher, M. Balasubramanian, B. R. Long, and M. M. Thackeray, *J. Electrochem. Soc.*, **161**, A318 (2014).
59. F. Friedrich, T. Zünd, A. Hoefling, J. Tübke, and H. A. Gasteiger, Manuscript in preparation.
60. T. B. Flanagan, C. N. Park, and D. H. Everett, *J. Chem. Educ.*, **64**, 944 (1987).
61. K. G. Gallagher, J. R. Croy, M. Balasubramanian, M. Bettge, D. P. Abraham, A. K. Burrell, and M. M. Thackeray, *Electrochem. commun.*, **33**, 96 (2013).
62. J. R. Croy, D. Kim, M. Balasubramanian, K. Gallagher, S.-H. Kang, and M. M. Thackeray, *J. Electrochem. Soc.*, **159**, A781 (2012).
63. K. Kleiner, B. Strehle, A. R. Baker, S. J. Day, C. C. Tang, I. Buchberger, F. F. Chesneau, H. A. Gasteiger, and M. Piana, *Chem. Mater.*, **30**, 3656 (2018).
64. P. M. Csernica, S. S. Kalirai, W. E. Gent, K. Lim, Y.-S. Yu, Y. Liu, S.-J. Ahn, E. Kaeli, X. Xu, K. H. Stone, A. F. Marshall, R. Sinclair, D. A. Shapiro, M. F. Toney, and W. C. Chueh, *Nat. Energy*, **6**, 642 (2021).
65. B. Strehle, K. Kleiner, R. Jung, F. Chesneau, M. Mendez, H. A. Gasteiger, and M. Piana, *J. Electrochem. Soc.*, **164**, A400 (2017).
66. R. A. House, G. J. Rees, M. A. Pérez-Osorio, J.-J. Marie, E. Boivin, A. W. Robertson, A. Nag, M. Garcia-Fernandez, K.-J. Zhou, and P. G. Bruce, *Nat. Energy*, **5**, 777 (2020).
67. G. Assat, D. Foix, C. Delacourt, A. Iadecola, R. Dedryvère, and J.-M. Tarascon, *Nat. Commun.*, **8**, 2219 (2017).
68. H. Liu, Y. Chen, S. Hy, K. An, S. Venkatachalam, D. Qian, M. Zhang, and Y. S. Meng, *Adv. Energy Mater.*, **6**, 1502143 (2016).
69. B. Qiu, M. Zhang, S.-Y. Lee, H. Liu, T. A. Wynn, L. Wu, Y. Zhu, W. Wen, C. M. Brown, D. Zhou, Z. Liu, and Y. S. Meng, *Cell Reports Phys. Sci.*, **1**, 100028 (2020).